

Varstrometry for Off-nucleus and Dual Subkiloparsec AGN (VODKA): Three Quadruply Lensed Quasars at Cosmic Noon in HST and JWST

MINGRUI LIU,¹ YU-CHING CHEN,¹ NADIA ZAKAMSKA,¹ XIN LIU,² YUE SHEN,² XUHENG DING,³ ARRAN C. GROSS,² HSIANG-CHIH HWANG,⁴ YUZO ISHIKAWA,⁵ AND KEDAR PHADKE²

¹William H. Miller III Department of Physics and Astronomy, Johns Hopkins University, Baltimore, MD 21210, USA

²Department of Astronomy, University of Illinois at Urbana-Champaign, Urbana, IL 61801, USA

³School of Physics and Technology, Wuhan University, Wuhan 430072, China

⁴Institute for Advanced Study, Einstein Dr., Princeton, NJ 08540, USA

⁵Kavli Institute for Astrophysics and Space Research, Massachusetts Institute of Technology, Cambridge, MA 02139, USA

ABSTRACT

We present results from imaging observations of three quadruply lensed quasars by Hubble Space Telescope (HST) and James Webb Space Telescope (JWST) at redshifts $z = 2.550$, 2.975 , and 1.500 . We model our targets assuming a singular isothermal ellipsoid mass profile and an elliptical Sérsic profile for the lensing galaxies, and reconstruct the geometric configuration of each system with measured Einstein radii of $0.44''$, $0.58''$, and $0.49''$. While no spectroscopic measurements are available for the lenses, we constrain the redshift of each lens to $0.5 < z < 1.2$, $1.0 < z < 1.5$, and $0.4 < z < 0.9$. For all three lenses, the best-fit light model yield a typical de Vaucouleurs $n_{\text{Sérsic}} \sim 4$ profile and an effective radius R_e around $\sim 1.5 - 3.5$ kpc. We accordingly classify the three lenses as early-type galaxies at an intermediate to high redshift, a common type for strong lensing galaxies. Compared to other known quadrupole lenses, the lensing galaxies in this work are at the lower end of the distribution of Einstein radii and upper end of the distribution of the lens redshifts. They represent an interesting quadrant of subarcsecond-separation lenses in the population of single-galaxy strong lensing which have been largely unexplored yet and will be great targets of interest in upcoming high-resolution lensing surveys.

1. INTRODUCTION

Ever since the first detection of strong gravitational lensing (Walsh et al. 1979), this relativistic phenomenon has been offering a unique perspective to various astrophysical and cosmological enigmas. For one, strong lensing serves as an effective probe for precision cosmology (Treu 2010; Saha et al. 2024). Time delay between photons from different lensed images enables high precision measurements on the Hubble constant H_0 , the expansion rate of the universe (Suyu et al. 2010; Treu & Marshall 2016). The H_0 value measured in the local Universe from distance ladders such as Type Ia supernovae (Riess et al. 2016, 2022) exhibits a $>3\sigma$ discrepancy with the value for early-stage Universe extrapolated from cosmic microwave background measurements (Planck Collaboration et al. 2020). Whether this tension originates from systematic uncertainties or implies new physics beyond the standard cosmic acceleration (Λ) with cold dark matter (Λ CDM) paradigm, such as exotic species of particle (Knox & Millea 2020) or early dark energy (Kamionkowski & Riess 2023), is still under investigation. As an independent probe for H_0 , strong

lensing offers precious insights about the nature of this ongoing Hubble tension (Suyu et al. 2010; Shajib et al. 2018; Riess et al. 2021).

Strong lensing could be a potential tracer for dark matter in galaxies. Presence of dark matter substructures at sub-galactic scales and along the line of sight affects the geometric configuration of strong lenses, manifested as abnormal positions or flux ratios of lensed images (Mao & Schneider 1998; Treu & Koopmans 2004; Dutton & Treu 2014). Microscopic physics of dark matter could imprint observable signatures in strong lensing systems. For example, self-interacting dark matter (Kaplinghat et al. 2014; Robertson et al. 2021) would modify the central density profile of lensing galaxy halos by conducting heat from the outskirts to the halo center that helps form a constant density core (Nishikawa et al. 2020; Gilman et al. 2023). Fuzzy dark matter (Hu et al. 2000; Schive et al. 2014) could create unique granular density core at the center of lensing halos, which would be distinct from that of any other kind of dark matter particle (Chan et al. 2020; Laroche et al. 2022).

Strong lensing provides a unique laboratory for understanding galaxy structure and evolution. Lensing,

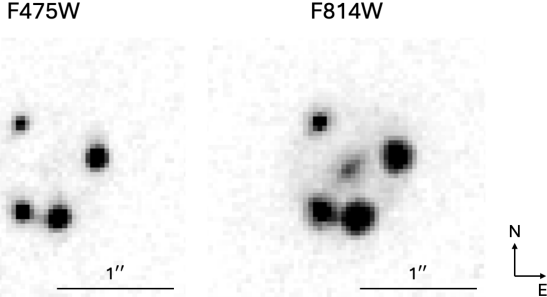


Figure 1. Images of J2218-3322 in the HST WFC3 F475W and F814W band.

often combined with stellar kinematics and photometry, probes mass structures of lensing galaxies, capable of decomposing them into stellar and dark matter constituents (Dutton & Treu 2014; Cappellari et al. 2015). It provides unique constraints on the mass distribution of galaxies at intermediate to high redshifts (Koopmans et al. 2006; Shajib et al. 2024). Large lens surveys such as the Sloan Lens ACS Survey (Bolton et al. 2006) and the BOSS Emission-Line Lens Survey (Bolton et al. 2012) have found the density profile of early-type galaxies generally follows a nearly isothermal power-law, which is consistent with the Λ CDM paradigm and reveals invaluable details into galaxy evolution across cosmic time (Koopmans et al. 2009; Sonnenfeld 2024).

By early 2020s, a few thousands strong lenses had been discovered (Metcalf et al. 2019; Huang et al. 2020). Many detections of strong lensing systems were serendipitous in surveys not designated for lenses. One population within which strong lenses often hide is the dual active galactic nuclei (AGNs), which are proposed progenitors of supermassive black hole (SMBH) mergers (Begelman et al. 1980; Shen et al. 2021, 2023). Before two SMBHs eventually coalesce following a galaxy merger, they spend hundreds of millions of years separated on sub-galactic scales (≤ 10 kpc; Hopkins et al. 2008; Chen et al. 2022). If both SMBHs are activated, a pair of AGN can then be observed simultaneously (e.g. Rodriguez et al. 2006; Liu et al. 2010; Shen et al. 2011). Such objects appear as two or more closely separated point sources and are difficult to distinguish from single quasars strongly lensed by a foreground galaxy. Varstrometry for Off-nucleus and Dual Subkiloparsec AGN (VODKA; Shen et al. 2019; Hwang et al. 2020) is a dedicated search program for dual quasars, with the goal to identify dual AGNs at high redshifts ($z > 1.5$) with subarcsecond separation from large all-sky surveys such as Gaia and Sloan Digital Sky Survey (SDSS). To date, VODKA has identified 150 dual AGN candidates,

with at least 15 of them suspected or already confirmed to be strong lenses (Chen et al. 2022; Gross et al. 2025).

In this work, we report imaging analysis of three quadruply lensed quasars: J221849.85-332244.2, MQJ080357.75+390823.0, and SDSSJ081331.27+25453.1 (hereafter J2218-3322, J0803+3908, and J0813+2545, respectively). We present detailed modeling and analysis of these three quadruply lensed systems in the following order: in Section 2, we introduce the selection and data reduction criteria for observations used in this work. In Section 3, we outline the details of our numerical modeling conducted. We then summarize the principal scientific findings in Section 4 and discuss their implications in Section 5. A final conclusion is drawn in Section 6. For this work, we adopt a flat Λ CDM cosmology with $\Omega_\Lambda = 0.7$, $\Omega_M = 0.3$, and $H_0 = 70$ km s $^{-1}$ Mpc $^{-1}$. All magnitudes are expressed in the AB system. Lenstronomy uses a “North up, East to the right” convention for displaying images, so all images are displayed in this way.

2. OBSERVATIONS & DATA REDUCTION

2.1. Target Selection

One of our targets, J2218-3322, was observed with the Wide Field Camera 3 (WFC3) on HST. The other two sources, J0803+3908 and J0813+2545, were observed with the Near Infrared Camera (NIRCam) on JWST.

J2218-3322 was selected to be observed by HST initially as a dual quasar candidate in the VODKA program. It was identified as a photometric quasar in both Wide-field Infrared Survey Explorer (WISE; Mateos et al. 2012; Secrest et al. 2015) and Panoramic Survey Telescope and Rapid Response System Telescope #1 (Pan-STARRS1; Chambers et al. 2016) data. However, in Gaia this target matches with two sources within 3'' of each other, with a Gaia G-band magnitude of 20.66 mag and 20.17 mag, as well as a Gaia `astrometric_excess_noise` property of 7.320 mas and 5.016 mas. As a result, Chen et al. (2022) identify it as a candidate dual or lensed quasar and use HST imaging to demonstrate that the morphology is consistent with a quadrupole lens. With optical spectra from Gemini Multi-Object Spectrographs and Space Telescope Imaging Spectrograph (STIS) on HST, Chen et al. (2025) determine a spectroscopic redshift of the lensed quasar (source) to be $z = 2.550$. The lensing galaxy of this system has not been analyzed in any previous work, and no spectroscopic or photometric redshift of it is available at present.

J0803+3908 and J0813+2545 are known quadruply lensed quasars. They are targets in the JWST

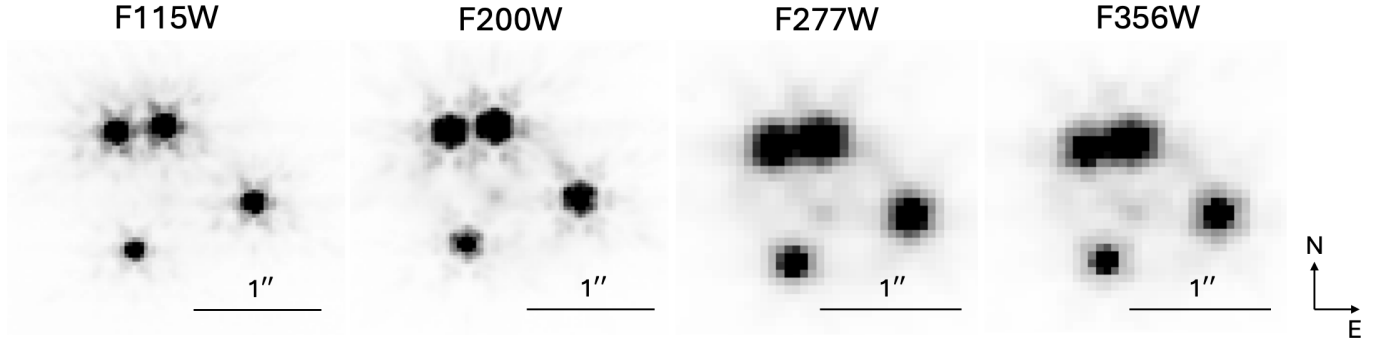


Figure 2. Images of J0803+3908 in the JWST NIRCam F115W, F200W, F277W, and F356W band.

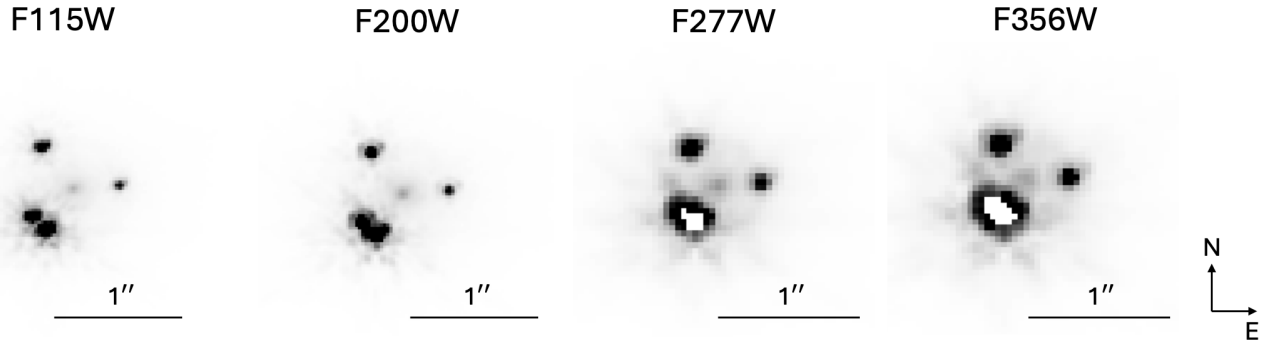


Figure 3. Images of J0813+2545 in the JWST NIRCam F115W, F200W, F277W, and F356W band. Voids in the two long filters are saturated pixels blanked out during data reduction.

Cycle 2 program GO-4204 (PI: Chen) to investigate small-separation dual quasars and lensed quasars. J0803+3908 is a confirmed lensed quasar in Gaia DR2 found by the dedicated survey for gravitationally lensed quasars in the Gaia catalog first conducted by Lemon et al. (2017). Schindler et al. (2018) report a spectroscopic redshift of $z = 2.975$ for the source quasar. J0813+2545 is a quad lens found serendipitously by Reimers et al. (2002) (who refer to this target as HS 0810+2554) when target acquisition images on HST/STIS captured the signature lensing configuration of this system. The modern quality of NIRCam imaging data compensates for the limited resolution and short exposure time (12 seconds) of the original images, thus better serving our scientific goal. The Hamburg All Sky Bright QSO Surveys (Hagen et al. 1995; Reimers & Wisotzki 1997) report a spectroscopic redshift of the source quasar at $z = 1.500$ (Hagen et al. 1999; Reimers et al. 2002). Recently this system has been observed in the radio C and Ku bands by the Very Large Array as a part of the VLA/24B-361 program (PI: Gross). Corresponding analysis (coming up in Baltaci et al. 2026, in prep.) indicates that in both bands the lensing geometry is seen as expected, but in the C-band there is blending between the two closest separated nodes. No radio emis-

sion from the central lensing galaxy is detected. Redshift of the lens galaxy in neither target is known.

2.2. *HST Target*

Chen et al. (2022) present HST/WFC3 imaging observations of J2218-3322, using the F475W (pivot wavelength $\lambda_p = 4772 \text{ \AA}$; effective width = 1344 \AA) and F814W ($\lambda_p = 8024 \text{ \AA}$; effective width = 1536 \AA) filters in the UV/Visible channel (UVIS). These data were obtained as part of the HST Cycle 27 program SNAP-15900 (PI: Hwang), carried out on August 21st, 2020 Universal Time (UT), with an exposure time of 360 seconds for the F475W band and 400 seconds for the F814W band. Each filter has a field of view of $20.5'' \times 20.5''$, resulting from a 512×512 pixel array where each pixel is $0.04''$. The data was processed with the standard HST data reduction pipelines. Images were first corrected for distortion and pixel effects. Next the dithered frames are reduced for cosmic rays and hot pixels then combined, and finally calibrated both photometrically and astrometrically with `calwf3` and `MultiDrizzle`.

2.3. *JWST Targets*

JWST/NIRCam observations of J0803+3908 and J0813+2545 sources were performed as parts of the JWST Cycle 2 program GO-4204 (PI: Chen).

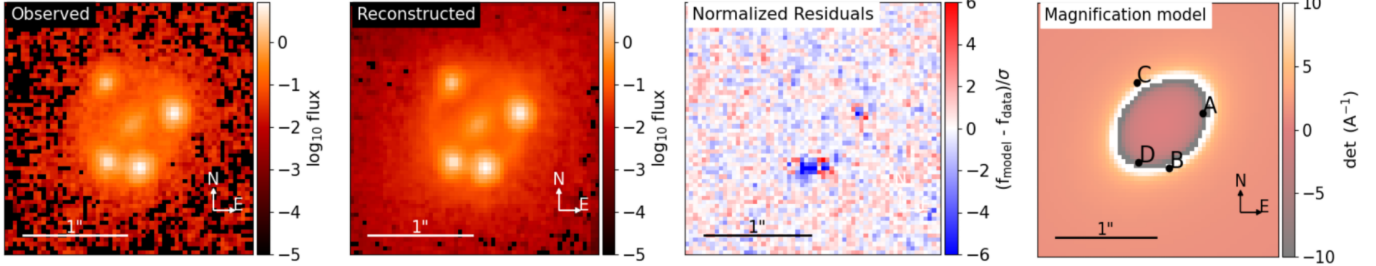


Figure 4. Best-fit models for J2218-3322 with `Lenstronomy` in the F814W band. Each panel from left to right presents the observed image, the reconstructed image, the normalized residual map, and the magnification map.

Parameter	J2218-3322	J0803+3908	J0813+2545
θ_E ('')	$0.44^{+0.00}_{-0.00}$	$0.58^{+0.00}_{-0.00}$	$0.49^{+0.00}_{-0.00}$
R_e ('')	$0.30^{+0.02}_{-0.02}$	$0.35^{+0.07}_{-0.03}$	$0.45^{+0.01}_{-0.01}$
$n_{\text{Sérsic}}$	$4.24^{+0.30}_{-0.18}$	$4.10^{+0.08}_{-0.12}$	$3.37^{+0.18}_{-0.09}$
q	$0.61^{+0.03}_{-0.03}$	$0.77^{+0.02}_{-0.02}$	$0.91^{+0.00}_{-0.00}$
ϕ (°)	$42.61^{+1.21}_{-1.21}$	$-22.54^{+2.26}_{-2.26}$	$13.28^{+0.00}_{-0.00}$
Lens Δx ('')	$0.05^{+0.00}_{-0.00}$	$-0.03^{+0.00}_{-0.00}$	$0.01^{+0.00}_{-0.00}$
Lens Δy ('')	$0.06^{+0.00}_{-0.00}$	$0.02^{+0.00}_{-0.00}$	$0.01^{+0.00}_{-0.00}$
Image A Δx ('')	$0.44^{+0.00}_{-0.00}$	$-0.25^{+0.00}_{-0.00}$	$-0.39^{+0.00}_{-0.00}$
Image A Δy ('')	$0.16^{+0.00}_{-0.00}$	$-0.37^{+0.00}_{-0.00}$	$-0.28^{+0.00}_{-0.00}$
Image B Δx ('')	$0.11^{+0.00}_{-0.00}$	$0.57^{+0.00}_{-0.00}$	$0.47^{+0.00}_{-0.00}$
Image B Δy ('')	$-0.36^{+0.00}_{-0.00}$	$0.00^{+0.00}_{-0.00}$	$0.03^{+0.00}_{-0.00}$
Image C Δx ('')	$-0.21^{+0.00}_{-0.00}$	$-0.39^{+0.00}_{-0.00}$	$-0.30^{+0.00}_{-0.00}$
Image C Δy ('')	$0.34^{+0.00}_{-0.00}$	$0.54^{+0.00}_{-0.00}$	$0.41^{+0.00}_{-0.00}$
Image D Δx ('')	$-0.20^{+0.00}_{-0.00}$	$-0.02^{+0.00}_{-0.00}$	$-0.26^{+0.00}_{-0.00}$
Image D Δy ('')	$-0.31^{+0.00}_{-0.00}$	$0.59^{+0.00}_{-0.00}$	$-0.41^{+0.00}_{-0.00}$

Table 1. Best-fit values of parameters with uncertainties for the lens mass and light models of each quadruply lensed quasar system from `Lenstronomy`. From top to bottom: Einstein radius θ_E , effective radius R_e , Sérsic index $n_{\text{Sérsic}}$, minor-to-major axis ratio q , position angle ϕ , centroid positions of lens and each lensed image Δx and Δy (defined as displacements from image center).

J0803+3908 was observed with two short filters F115W ($\lambda_p = 1.154 \mu\text{m}$; bandwidth $\Delta\lambda = 0.225 \mu\text{m}$) and F200W ($\lambda_p = 1.988 \mu\text{m}$; $\Delta\lambda = 0.463 \mu\text{m}$), as well as two long filters F277W ($\lambda_p = 2.776 \mu\text{m}$; $\Delta\lambda = 0.673 \mu\text{m}$) and F356W ($\lambda_p = 3.566 \mu\text{m}$; $\Delta\lambda = 0.786 \mu\text{m}$) on April 17th, 2024 UT. J0813+2545 was observed with the same four bands on March 29th, 2024 UT. The nominal pixel scale is $0.031''/\text{pixel}$ for the short filters and $0.06''/\text{pixel}$ for the long filters, with the point-spread function (PSF) FWHM of $0.07''$ at $2 \mu\text{m}$ for the short and $0.13''$ at $4 \mu\text{m}$ for the long filters. All bands share the same field of view of $2.2' \times 2.2'$. The data were reduced with the JWST Calibration Pipeline package in version 1.18.0 and CRDS Context file `jwst_1364.pmap`. We follow most of the standard procedures except for two customizations: i) the `clean_flicker_noise` step was

turned on in Stage 1 in order to correct for the $1/f$ noise that produces the striping patterns in the original images; ii) the `suppress_one_group` property in the `ramp_fit` step in Stage 1 was turned off to recover bright pixels at the center of certain quasar images that were saturated after integration in Frame 1 and masked out by the default pipeline settings. Turning off the flag preserves these pixels in following reduction stages and the final data product. This, however, cannot retrieve pixels saturated before Frame 1, which are the voids seen in Fig. 3.

3. MODELING

For fitting the quadruply lensed quasars, we utilize `Lenstronomy` (Birrer & Amara 2018), an open-source python-based software for numerically modeling gravitational lensing systems. It offers a high level of flexibility in choices of models for the mass distribution of the lens, as well as light profiles for the lens and the source. The best-fit parameters in the models are acquired with numerical techniques such as the particle swarm optimization or Markov chain Monte Carlo algorithm.

3.1. Lens Mass Profile

The mass distribution of a galaxy can often be modeled by an elliptical mass density distribution (Treu & Koopmans 2004; Dutton & Treu 2014). One of such models is the singular isothermal ellipsoid (SIE; Kormann et al. 1994a), which has been verified on a wide selection of strong lensing galaxies (Bolton et al. 2008; Capellari et al. 2015). This profile represents a 3D mass density profile that radially decays as a power law on ellipsoid of rotation with semi-major axes r : $\rho \propto r^{-\gamma}$, with a power-law slope $\gamma = 2$ (Auger et al. 2010). We adopt this in `Lenstronomy` to model the total mass (both baryons and dark matter) of our lens samples. In lensing-related literature, this model is often reduced to the surface mass density or “convergence”:

$$\kappa(\theta_1, \theta_2) = \frac{3 - \gamma}{2} \left(\frac{\theta_E}{\sqrt{q\theta_1^2 + \theta_2^2/q}} \right)^{\gamma-1} \quad (1)$$

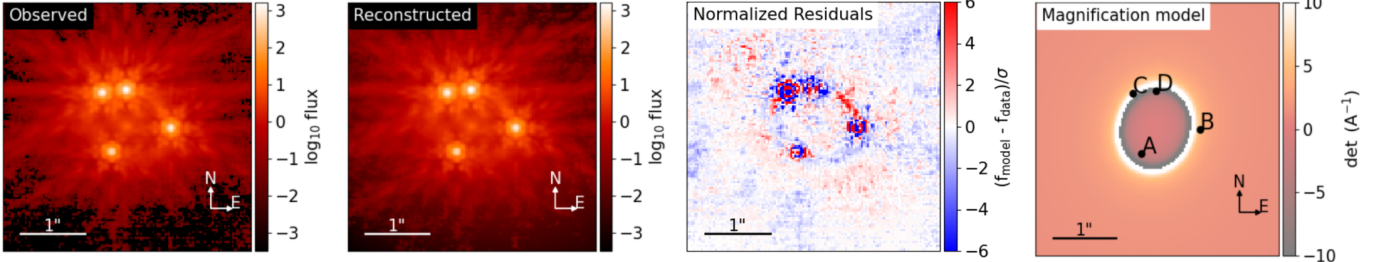


Figure 5. Best-fit models for J0803+3908 with Lenstronomy in the F200W band. Panels are arranged in the same convention as in Fig. 4.

where θ_1, θ_2 are coordinates aligned with the major and minor axes of the projected ellipse rotated from sky-plane coordinates with a position angle ϕ of the rotated coordinate system, q is the minor-to-major axis ratio, θ_E is the Einstein radius of the lens, and power-law index γ is fixed at 2 in our modeling (Tessore & Metcalf 2015; Schmidt et al. 2023). This quantity is also a dimensionless ratio $\kappa = \sum / \sum_{\text{crit}}$, where \sum is the lens' projected mass density on the lens plane, and $\sum_{\text{crit}} = \frac{c^2}{4\pi G} \frac{D_S}{D_L D_{LS}}$ is the critical surface mass density, where D_L, D_S, D_{LS} are the angular diameter distance to the lensing galaxy, the source quasar, and that between the two, respectively. Multiple lensed images of the source can only be observed when the lens' \sum exceeds the critical value (Saha et al. 2024).

In addition, other perturbers, such as galaxies or clusters either nearby or along the line of sight (Kochanek & Apostolakis 1988), large-scale structures (Bar-Kana 1996), or even complicated structures within the lensing galaxy (Etherington et al. 2024) might disturb the lensing potential and consequently contribute to the inferred mass profile of the lens or introduce shear. We have an additional shear term which had little effects on the final goodness-of-fit and best-fit parameter values. We thus conclude that none of the quads are subject to significant external shears and report best-fit models without shears.

3.2. Lens & Source Light Profile

For the light (i.e. surface brightness) profile of the lens and the source, we adopt Sersic (1968) models. Their 1D projection along the radial direction is characterized as

$$I(R) = I_e \exp \left(-b_n \left[\left(\frac{R}{R_e} \right)^{\frac{1}{n}} - 1 \right] \right) \quad (2)$$

with $b_n \approx 1.999n - 0.327$, where R_e is the half-light/effective radius of the lens, n is the Sérsic index, and I_e is the surface brightness at the effective radius i.e. $I_e = I(R_e)$ (Schmidt et al. 2023).

For the lens, to account for its possible ellipticity, the radius $R = \sqrt{q\theta_1^2 + \theta_2^2}/q$ features coordinates θ_1 and θ_2 as well as axis ratio q all defined in the same conventions as in κ above. The position angle of the ellipse is another fitted parameter in the model. We do not enforce these position and ellipticity terms to be identical in the mass and light profile, as we fit the two profiles separately with no assumption on whether these two profiles for our lenses trace each other in morphology. Our fitting experiments suggest these geometry parameters in the light profile are very similar to those in the mass profile.

When axis ratio q is fixed at 1, the elliptical profile reduces to a spherical Sérsic model. We model the light profile of the source quasar's host galaxy with this spherical profile, and the light component of the quasar with a delta function. The Sérsic index is bounded in between 1 and 6 to avoid non-physical results.

3.3. PSF Model

To obtain a realistic fit of the lenses, Lenstronomy requires a model of the point spread function (PSF) for the instrument that produces the input images, which are convolved with the model light profiles to reproduce the observed data. For J2218-3322, due to the undersampled nature of WFC3 images, a precise analytical PSF of the detector is difficult to acquire. Rather, it is common to extract an empirical PSF model from a different object than the target in the same image, usually a nearby field star. No star is in the field of J2218-3322 that has sufficient brightness necessary for our science goal. Instead, we employ an empirical PSF extracted from an object observed by the same WFC3 filter with a similar exposure time in an archival data hosted on the Mikulski Archive for Space Telescopes (MAST; file ID: 1329728, originally from HST program GO-15986, PI: Mutchler). For J0803+3908 and J0813+2545, both fields have very few bright stars with only the brightest one showing satisfactory quality, thus we extract the brightest star in each of the fields and set them as the sample PSF model.

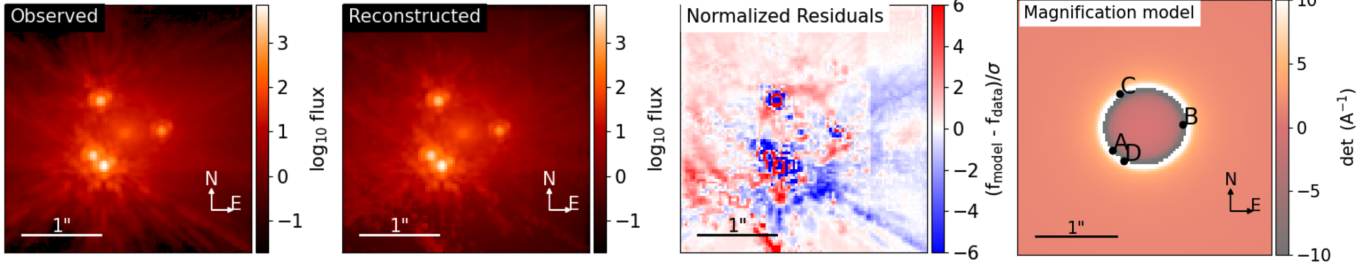


Figure 6. Best-fit models for J0813+2545 with Lenstronomy in the F200W band. Panels are arranged in the same convention as in Fig. 4.

3.4. Noise Properties

Lenstronomy searches across the parameter space for the best-fit parameters that yield the maximum likelihood, and evaluates the goodness-of-fit using the reduced chi-square parameter χ^2_ν , where $\chi^2_\nu \sim 1$ indicates a good fit. For that, it requires the noise/uncertainty in the inputted image data as an initial parameter. For HST data, we identify two dominant sources of uncertainty: the background, and the Poisson noise. We calculate the background rms noise σ_{rms} by sampling multiple background regions (blank areas without any bright objects) across the image field and extracting the median of their root mean square (rms) values. The Poisson noise is the shot noise of the detector, which we evaluate as $\sigma_{\text{Poi}} = \sqrt{N}$ with N being the number of electrons detected during an exposure. The total uncertainty is then the quadratic sum of both noises: $\sigma_{\text{tot}} = \sqrt{\sigma_{\text{rms}}^2 + \sigma_{\text{Poi}}^2}$.

By default, NIRCam data cubes include a data array (the `ERR` extension in the FITS file) that contains the uncertainty for each pixel value of the science product. It is calculated as the standard deviation combining variance for the Poisson noise σ_{Poi}^2 , variance for the detector read out noise σ_r^2 , and variance for the flat-field noise σ_{ff}^2 i.e. $\sigma_{\text{ERR}} = \sqrt{\sigma_{\text{Poi}}^2 + \sigma_r^2 + \sigma_{\text{ff}}^2}$, to which we add the median background rms value σ_{rms} calculated by `photutils` during background subtraction in quadrature to obtain the final total uncertainty $\sigma_{\text{tot}} = \sqrt{\sigma_{\text{rms}}^2 + \sigma_{\text{ERR}}^2}$.

3.5. Model Robustness

In addition to the SIE mass model introduced above that describes the total mass of a galaxy, we also experiment with a “composite” model, which characterizes the baryon and dark matter in a lens with two distinct profiles. For the baryonic/luminous mass i.e. the stellar halo, we adopt a Hernquist (1990) model. For the dark matter halo, we choose a Navarro-Frenk-White (NFW; Navarro et al. 1997) profile. Both models in their original forms require spherical symmetry and fall short of accounting for ellipticity in realistic halos. Thus, we utilize a modified version for the two proposed by Oguri (2021), which uses cored steep ellipsoids (CSE; Keeton &

Kochanek 1998; Keeton 2001) to approximate an elliptical Hernquist and NFW halo. Such a composite model, when converged properly, yields very similar results to that from the SIE model, including the Einstein radius, ellipticity, and centroid position of a lens. We do not include results from this alternative model because with the composite model, two consecutive trials of fitting the same target with the same set of input parameters sometimes produce significantly different outcomes, especially parameters of the stellar halo profile. Certain parameters are more robust than others. We observe that for the same lens being modeled, the Einstein radius is usually the most stable and rarely changes across trials, followed by centroid positions that could change by $\sim 0.005''$ each trial, with ellipticity being the least robust parameter that would occasionally vary by more than 10% in different trials. Fits using the SIE model demonstrate a similar hierarchy of parameter robustness: Einstein radius $>$ centroid position $>$ ellipticity. The magnitude of this run-to-run variability, especially for the ellipticity terms, exceeds the fitting uncertainties reported in Table 1. We warn that exact ellipticity (and possibly orientation) of the mass model might be uncertain.

4. ANALYSIS

4.1. Imaging & Modeling Results

In this section we present imaging analysis and Lenstronomy modeling results of the three quads.

4.1.1. J2218-3322

Fig. 1 displays the WFC3 images of J2218-3322 in the F475W and F814W bands. This system consists of four point-like sources surrounding a central extended object, a classic geometry for a background quasar strongly lensed into quadruple images by a foreground galaxy. The central lensing galaxy appears as a compact object elongated along the northeast-southwest direction. This morphology is more likely being indicative of its early-type nature (discussed in Sec. 5) than being due to lensing. It is more evident in the F814W band while barely

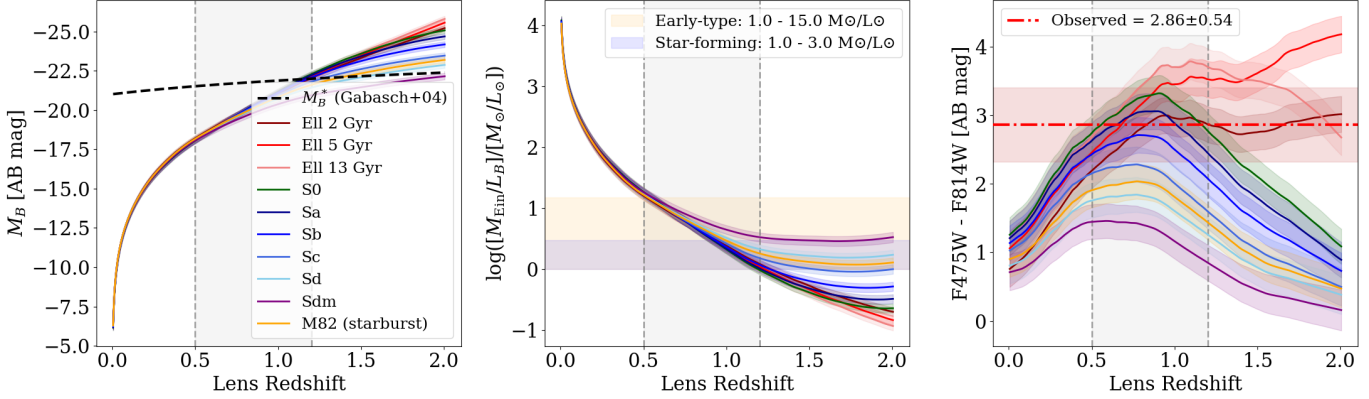


Figure 7. Photometry analysis of J2218-3322’s lens. Left to right: rest-frame B-band luminosity (in AB mag), B-band mass-to-light ratio, and WFC3 [F475W - F814W] color. Black dotted line lays out B-band characteristic luminosity of early-type galaxies at intermediate redshifts reproduced from [Gebasch et al. \(2004\)](#). Shaded regions near each curve indicates the relative size of associated uncertainty. Vertical dotted gray lines mark the range of most probable redshift for this lens between $0.5 < z < 1.2$.

visible in the F475W band. Enclosing the central object is a very faint Einstein ring, which again is brighter in the redder filter, and the four lensed quasar images are positioned on the Einstein ring. The brightest image is at the lower right of the field, while the faintest is at the upper left.

Fig. 4 presents the `Lenstronomy` best-fit results for the system in the F814W band. We consider this band to be more informative for `Lenstronomy` as the lens has a larger flux in it and perform fitting with it. The fit produces a good reconstruction of the system that is morphologically very similar to the original image. The normalized residual map illustrates a pattern that appears as a random distribution spatially. At most pixels, the fitted flux value deviates from the actual value by $\leq 3\sigma$. This reinforces the reliability of the fit, along with the best-fit $\chi^2_\nu = 1.21$. The fitted magnification model suggests the point source B should be the brightest and A the dimmest, which disagrees with the observation. Such a mismatch of magnification is a long known issue in numerical modeling of strong lensing systems. This so-called flux ratio anomaly could be attributed to mass fluctuations caused by structures at sub-galactic scales that distorts the lensing potential, for example, dark matter halos, for which a smooth mass profile like the SIE model cannot fully account. This might imply the existence of prominent dark matter substructures within the halo of the lens ([Vegetti et al. 2024](#)). Microlensing by individual stars and dust extinction could contribute to such anomalies as well ([Schechter & Wambsganss 2002](#); [Keeton et al. 2006](#)). Accounting for such flux ratio anomalies in strong lenses is a challenging task, as warned by many (e.g. [Schechter 2003](#)). We thus refrain from putting forth extensive investigation on this issue and warn that this fitted model might not be trustwor-

thy. The best-fit values of important model parameters are summarized in Table 1. The results suggest an Einstein radius of $0.44''$.

4.1.2. J0803+3908

Fig. 2 shows the NIRCam images of J0803+3908 in the F115W, F200W, F277W, and F356W filters. It includes five point sources, including four bright lensed images and a dim foreground lens that exhibits a circular shape. A faint Einstein ring exists as well, which is more apparent in the long-wavelength filters than in the short ones. Two lensed images on the northwest of the images sit closely to each other with the one on the east being the brightest. The dimmest one is at the lower left of the field.

Fig. 5 lays out the `Lenstronomy` fit for J0803+3908 in the F200W band. We choose this band to be the most informative for i) the short-wavelength filter has a better angular resolution than the long-wavelength filters, and ii) the lens flux is larger than that in F115W. The reconstructed image is visually similar to the original observation, with a best-fit $\chi^2_\nu = 3.87$. There are significant ($\geq 6\sigma$) residuals around each of the four lensed images, with a concentric ring-like pattern. This implies that the PSF model we extract from the field star might be suboptimal to fully characterize the PSF structures of the observed images. The sample field star from which we extract the PSF model is dimmer than all four lensed images, potentially causing the model to have insufficient information on diffraction spikes and speckles to model the brighter images. The two top images being too close to each other might have led to partial overlap of their PSFs, which could make the fitting even more challenging. We have experimented with other options, such as empirical PSF models from other works or simulated PSF models generated by STPSF ([Perrin et al.](#)

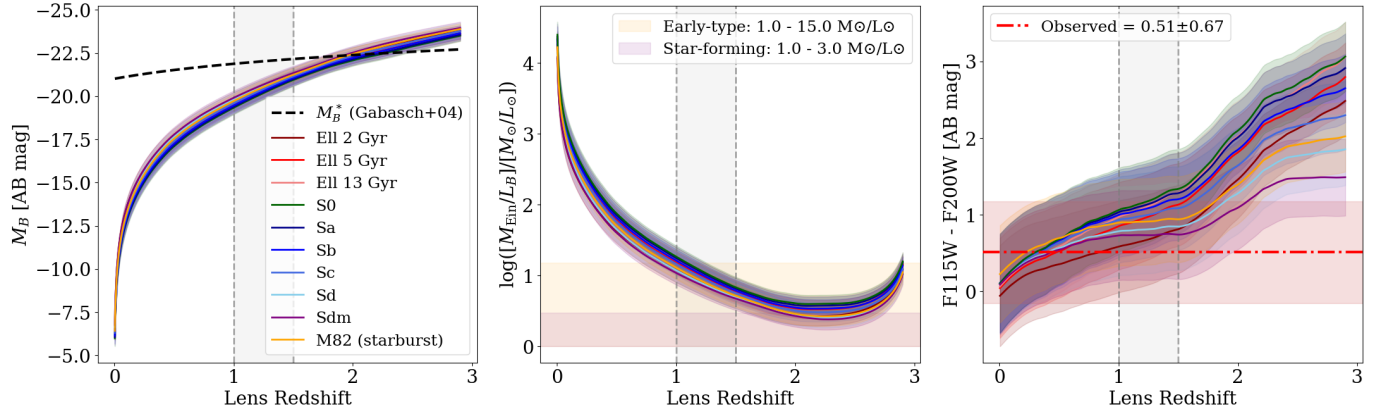


Figure 8. Photometry analysis of J0803+3908’s lens. Panels are arranged in the same convention as in Fig. 7 while third panel shows the NIRCam [F115W - F200W] color. Range of most probable redshift for this lens is between $1.0 < z < 1.5$.

2012), which all struggle to give a better portrait of the complicated diffraction pattern of NIRCam. Nonetheless, the high residuals are near the point sources, and the rest of the fit is reliable. The fitted magnification model, similar to that for J2218-3322, shows a noticeable discrepancy with the observed flux ratios between images and might be not reliable. The other best-fit parameters are in Table 1. The fit yields a Einstein radius of $0.58''$.

4.1.3. *J0813+2545*

Fig. 3 illustrates the NIRCam images of J0813+2545 in the four NIRCam filters, displaying a dim central lensing object surrounded by four brighter lensed images. The lens of this system is visually distinguishable in all four filters, enclosed by a dim Einstein ring. Two overlapping bright images are located on the southwest of the image field. In the two long-wavelength filters, pixels at the centers of quasar image are very bright and saturated, causing them to be blanked out by the data reduction pipeline and are non-recoverable.

Fig. 6 demonstrates the numerical fit results for J0813+2545 from **Lenstronomy** in the most informative F200W band. The image reconstruction yields a best-fit $\chi^2_\nu = 4.56$. We observe the ring-like patterns near point sources, indicative of a similar PSF mismatch. The positive residual patterns spanning a wide region on the top of the field is indicative of potential issue of excessive background noises. Fitted values of model parameter for J0813+2545 are in Table 1. This system has a best-fit Einstein radius of $0.49''$.

4.2. *Constraints on Lens Redshift*

As no spectroscopic measurements on the lensing galaxies are available at present, we utilize our **Lenstronomy** fit results to constrain the redshift range for each of the lenses by examining properties of the

lensing galaxies, namely mass, luminosity, and color, as a function of redshift, to determine the redshift at which these quantities have the most probable values.

The total mass (for both baryonic and dark matter) enclosed within the Einstein radius θ_E of a strong lens M_{Ein} is:

$$M_{\text{Ein}} = \frac{c^2}{4G} \frac{D_L D_S}{D_{LS}} \theta_E^2, \quad (3)$$

where D_L , D_S , D_{LS} are the angular diameter distance to the lensing galaxy, the source quasar, and that between the two, respectively, all of which are dependent on lens redshift z_L (Saha et al. 2024). Therefore, we can evaluate the total enclosed mass as a function of redshift $M_{\text{Ein}}(z_L)$.

In addition to the enclosed mass, given the light profile fitted by **Lenstronomy**, we can evaluate the luminosity enclosed within a lensing galaxy’s Einstein radius as a function of z_L . For each lens, we reconstruct its surface brightness profile with the best-fit light model parameters. Then, we integrate the surface brightness within the Einstein ring to obtain the total enclosed spectral flux density in unit of Jansky. For the HST target, as it was observed in the F475W and F814W filter, we obtain the enclosed flux densities in both bands. To derive the corresponding total luminosity, we need to integrate the flux density over the lensing galaxy’s spectral energy distribution (SED). Since the exact Hubble type of the lenses are unknown, we select 10 candidate SED templates of different galaxy types from the SWIRE template library (Silva et al. 1998), including three elliptical galaxies with a synthetic stellar population at 2, 5, and 13 Gyr, six spiral galaxies of different types (Sa, Sb, Sc, Sd, S0, Sdm), as well as one starburst galaxy M82, all assuming a Salpeter (1955) initial mass function. For all SEDs, we calculate synthetic flux densities in two filters and normalize to the observed fluxes in these two filters using the least squares method. We integrate the SEDs

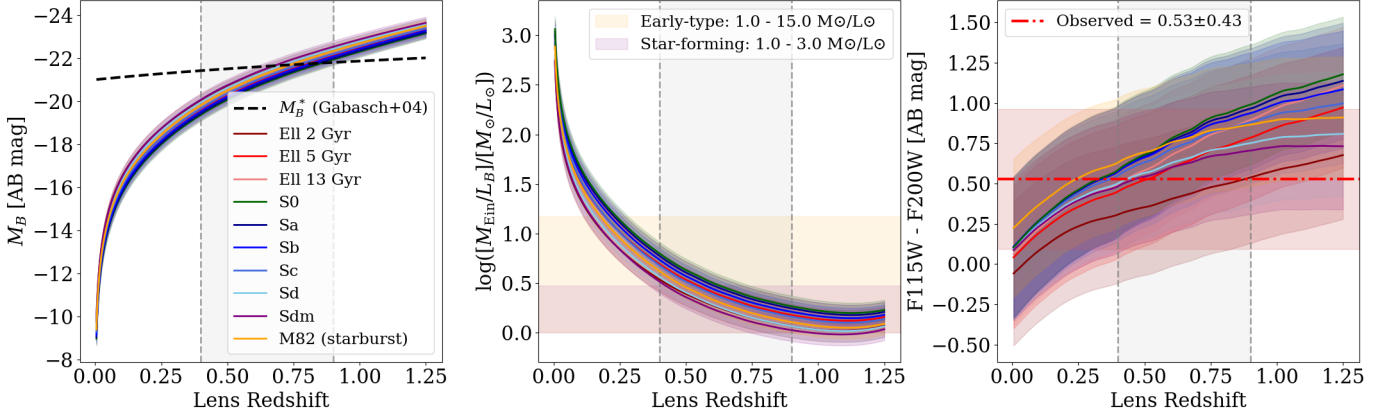


Figure 9. Photometry analysis of J0813+2545’s lens. Panels are arranged in the same convention as in Fig. 8. Range of most probable redshift for this lens is between $0.4 < z < 0.9$.

over the rest-frame B band (4000 - 5000 Å), a common benchmark for galaxy studies to obtain the enclosed flux of a lens, and subsequently derive the enclosed luminosity $L(z_L)$ as a function of lens redshift.

Now for every lens, we have both $M_{\text{Ein}}(z_L)$ and $L(z_L)$. Thus we can evaluate the mass-to-light ratio $[M_{\text{Ein}}/L](z_L)$ of a lens enclosed within the Einstein radius as a function of z_L . In addition, we have the synthetic colors of templates as a function of z_L . We compare it to the observed color of the lens and examine at what redshift(s) would the model-dependent color match the observed value.

We also evaluate the potential systematic uncertainties associated with the photometry results. To obtain a model-independent sanity check for lens galaxy colors, we develop an independent pipeline that fits the lens light with phenomenological models (e.g. 2D Lorentzian profile, comparable to a PSF-convolved Sérsic; this also accounts for the potential systematics induced by the PSF mismatch). We intend to be as agnostic as possible about the structural parameters of the lens and just double-check whether the flux given by Lenstronomy is physical. One potential pitfall of Lenstronomy fits is the software does not include a background in the lens light model, i.e. it assumes that the observed flux is entirely due to the source and the lens. While realistically those pixels might be subject to various contamination, including noise fluctuations, bright PSF spikes or source galaxy light leaking into the Einstein ring, etc. The flux/luminosity derived by Lenstronomy thus could have overestimated the lens light. Our custom pipelines examine the potential systematics induced by this assumption by fitting models both with and without a background. The former consists of a uniform background accounting for contaminating fluxes and a central profile for lens light. Derived flux from the central profile marks the lower bound of total enclosed flux

within Einstein radius. The without-background model, inheriting similar assumptions with Lenstronomy, sets the upper bound. We set the best estimate and associated uncertainty of lens flux to be the mean and standard error of these measurements at the 95% confidence level.

Fig. 7, 8, and 9 present the photometry results for the lens of J2218-3322, J0803+3908, and J0813+2545, respectively. The dotted black line in each B-band lens luminosity $M_B(z_L)$ plot displays an empirical relation between the B-band characteristic luminosity M_B^* and redshift z as $M_B^*(z) = -20.92 - 1.25 \ln(1+z)$ by Gobasch et al. (2004), as a reference for how is the lens luminosity compared to the “representative” value at a given redshift. We stop plotting out to higher redshifts once a lens’ luminosity surpasses local M_B^* value by $\sim 2 - 3$ magnitudes. The colored boxes in the enclosed mass-to-light ratio $[M_{\text{Ein}}/L_B](z_L)$ plots mark a range of typical mass-to-light ratios for different galaxy types cited from the literature (e.g. Graham 2002; van der Marel & van Dokkum 2007; Cappellari et al. 2013a). Those references report the dynamical mass-to-light ratios within $1 R_e$ of galaxies, that is, a few kpc within a galaxy’s center. The Einstein radius of a lens corresponds to different physical radii at different redshifts. For the lenses in this work, within the possible redshift range their Einstein radii are in between $\sim 1 - 3.5$ kpc, which are compatible with the reference values. We use $[M_{\text{Ein}}/L_B](z_L)$ and the redshift-dependent color ($[F475W - F814W](z_L)$ for HST target and $[F115W - F200W](z_L)$ for JWST targets) to constrain the most possible range of redshift for a lens: if i) the mass-to-light ratio of a certain galaxy model is within a reasonable range at a certain redshift, and ii) the color of the model is compatible with the observed value (model & observed color directly meet, or error bars overlap) at that redshift, we then conclude the lens could be that type of galaxy at that redshift. We

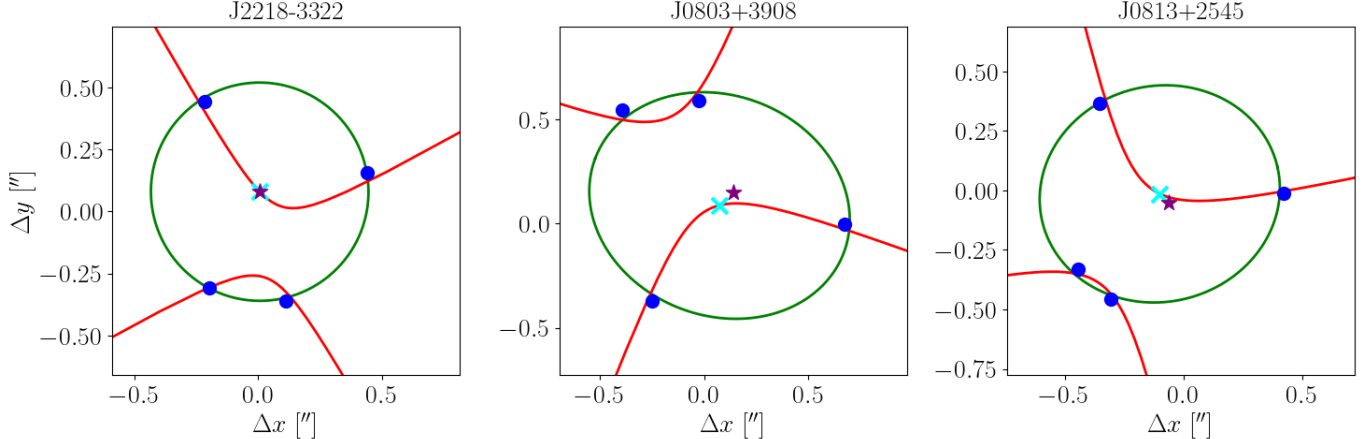


Figure 10. Fitting result for the three lensing systems in this work with the alternative model. Blue dots represent the lensed quasar images. Cyan crosses represent the fitted source position. Purple stars represent the fitted position of the center of the lensing potential.

report the constrained redshift range for each lens to be: J2218-3322: $0.5 < z < 1.2$; J0803+3908: $1.0 < z < 1.5$; J0813+2545: $0.4 < z < 0.9$. Implications from these constraints are discussed in Sec. 5.

4.3. Alternative Lensing Model

In this section we explore an alternative model for our systems – specifically, the singular isothermal elliptical lensing potential, one of the simplest models that produces a quadruple lens, following prescriptions by Witt (1996); Wynne & Schechter (2018); Luhtaru et al. (2021); Schechter & Luhtaru (2024). In this model, the two-dimensional lensing potential is

$$\psi(\theta_1, \theta_2) = b\sqrt{\theta_1^2 + \theta_2^2/q^2} \quad (4)$$

using the same notation as equation (1), i.e., θ_1 and θ_2 are measured along the major and minor axes of the lensing potential from the center of the lens. The convergence for this model $\kappa(\theta_1, \theta_2) \propto (\theta_1^2 + \theta_2^2)/(\theta_1^2 + \theta_2^2/q^2)^{3/2}$, i.e., similar to but not exactly the same as the convergence of the power-law ellipsoid with $\gamma = 2$ we explored with `Lenstronomy` (for which the analytical lensing potential is given by Meylan et al. 2006).

For this potential parameterized by the overall normalization b and ellipticity q , the four images must lie on an ellipse (“Wynne’s ellipse”, Wynne & Schechter 2018) centered on the projected (original, unlensed) source position x_S, y_S . They must also lie on a rectangular hyperbola, i.e., a hyperbola whose asymptotes are orthogonal to each other, which passes through both the center of the lens x_L, y_L and the projected source position x_S, y_S (“Witt’s hyperbola”, Witt 1996). Both the hyperbola and the ellipse have the same position angle θ_L which is the position angle of the long axis of the potential distribution, and they both have q as a shape parameter.

Additionally, the ellipse depends on the normalization of the lensing potential b . Therefore, the four positions of the images provide 8 data points $(x_i, y_i, i = 1\dots 4)$ to construct a 7-parameter model of the best-fitting Witt’s hyperbola and Wynne’s ellipse which yields all the parameters of the lensing potential and the unlensed position of the source.

In our implementation of the isothermal elliptical potential fit, we take the best-fitting image positions from our `Lenstronomy` fits and minimize the sum of the squares of the distances from the images to Wynne’s ellipse and Witt’s hyperbola to obtain the best-fitting model parameters. We require the Witt’s hyperbola to pass through the unlensed source position, but not necessarily the center of the lensing potential. This is inspired by the procedure by Schechter & Luhtaru (2024) who indicate that the center of lensing potential could be displaced from the hyperbola due to physical reasons that are discussed in Sec. 5.3. We experiment with two other fitting approaches, either requiring that the centroids of both the potential and the unlensed source position are on the hyperbola, or requiring none of the centroids to be on the hyperbola. These three recipes in principle should all reproduce the same lensing geometry, conditioned on that the true lensing potential is similar to the assumed analytical model. We find that only the first approach (fixing centroids of the source but not potential on the hyperbola) yields reasonable fits. This could imply that the lensing potential might be not well described by the model.

Overall we find that the positions of the images are fit well for all three targets in this work as shown in Fig. 10, reproducing them within $\sim 0.01 - 0.03''$ from the Wynne’s ellipse or the Witt’s hyperbola, which are $\sim 3\% - 7\%$ of their lenses’ Einstein radii. The structural

parameters yielded from this model are not consistent with the values fitted by `Lenstronomy`. The lens and source positions fitted by each model differ by $\sim 0.05''$. The axis ratios differ by up to ~ 0.3 , and the position angles are discrepant by at most $\sim 60^\circ$.

Such a discrepancy could be another implication that the true lensing potential is more complicated than that assumed by the analytical model. The potential adopted by `Lenstronomy`, which reproduces better fits of lensed image positions, could be more loyal to reality than the Witt / Wynne model. Besides, this analytical model is essentially geometric; it fits the structural parameters of the lensing potential only using the lensed image positions. `Lenstronomy` fits more information (mass & light, magnification, quasar host galaxy etc.) with the input image. While the lensing potential adopted by both models are similar, the data being fitted might not be necessarily the same. This makes a stronger case for the above, as the Witt / Wynne model fits solely the image positions and does not reproduce the geometry well, whereas `Lenstronomy` fits more quantities simultaneously and yet reproduces the positions of the PSFs well. These differences could also be attributed to the fact that the structural parameters of the lenses could be in fact not well constrained. As stated in Sec. 3.5, parameters in `Lenstronomy` fits show a "hierarchy of errors" with the ellipticity terms (axis ratio and position angle) being the most poorly determined.

5. DISCUSSION

5.1. *Classifications & Properties of Lenses*

Strong lensing galaxies detected until now are biased towards a specific type: bright, compact, massive early-type galaxies at an intermediate redshift ($z \leq 1$). A galaxy can act as a strong lens only when its surface mass density reaches or exceeds the critical threshold Σ_{crit} . This condition favors galaxies with more mass and more compact geometry. Besides, major brightness-limited lens surveys tend to select more luminous galaxies (Sonnenfeld et al. 2023; Sonnenfeld 2024). Due to these selection effects, compact massive early-type galaxies overwhelmingly dominate the documented population of strong lensing galaxies (Auger et al. 2009; Sygnet et al. 2010). Late-type/star-forming galaxies, while more numerous, are far less common among lenses, accounting for only $\sim 10\% - 20\%$ of all lenses with a substantially lower lensing cross-section than early-types (Keeton et al. 1998; Keeton & Kochanek 1998). Out of 40 lensing galaxies in quadruply lensed quasars with known lens redshift documented as of October 2025 (see Appendix), 33 have classifications of galaxy types reported, among which 27 have been classified or sus-

pected as early-type galaxies, while only 6 are claimed to be late-type/spiral galaxies.

The three lenses in our sample are likely early-type galaxies as well. We measured the Sérsic index for each lens to be 4.24, 4.10, and 3.37, i.e. all consistent with a de Vaucouleurs $n_{\text{Sérsic}} = 4$ light profile for elliptical/early-types. The best-fit effective radii for these lenses are $0.30''$, $0.35''$, and $0.45''$. At their respective redshift ranges, the corresponding physical distances are around 1.5 - 3.5 kpc. For massive early-types of $\sim 10^{10} - 10^{11} M_\odot$ at $z \leq 1$, the typical R_e is in between 1 - 5 kpc (e.g. Cappellari et al. 2013b; van der Wel et al. 2014). The three lenses thus fit comfortably into the mass-size plane for early-type galaxies.

J2218-3322 exhibits a significant redness. While dust extinction and/or external reddening cannot be ruled out, it is a strong indicator of a passively evolving galaxy i.e. early-type, consistent with the previous classification. J0803+3908 and J0813+2545 show bluer colors, which is less common for early-type galaxies that have evolved and show little to no ongoing star formation. Certain scenarios might account for such an observation. Some elliptical and S0s contain substantial cold gas reservoirs, either from recent gas-rich mergers or ongoing accretion, that boost star formation rates (e.g. Combes et al. 2007). Recent major mergers can trigger starbursts in early-types, particularly in the transition phase, causing a temporarily blue-ward shift in color (e.g. George 2017).

Though similar in color, the two JWST lenses have significantly different B-band luminosities. J0813+2545 is brighter than J0803+3908 by roughly 2 magnitudes across the most likely redshift range. At the highest possible redshift, it surpasses the local L^* by about 1 magnitude. Yet J0803+3908 is always below L^* at its maximum possible brightness. Early-type galaxies are known to be very bright objects with luminosities near or over L^* . Massive yet under-luminous early-type galaxies are not unprecedented, and several formation pathways are available to explain these type of objects. When baryons at the centers of dark matter halos cool, dark matter is believed to respond by undergoing adiabatic contraction, which leads to the contraction of the dark matter halo and amplifies the central dark matter density (Gnedin et al. 2004; Li et al. 2022). At inner regions of a galaxy, the elevated dark matter proportion could undermine the stellar population's contribution to the total mass. In addition to the central cusps, dark matter substructures could grow up to $10^9 M_\odot$ (Hezaveh et al. 2016), which might dominate over stellar mass within small radii like those \sim kpc regions within Einstein radii. Besides, strong lensing early-type galaxies

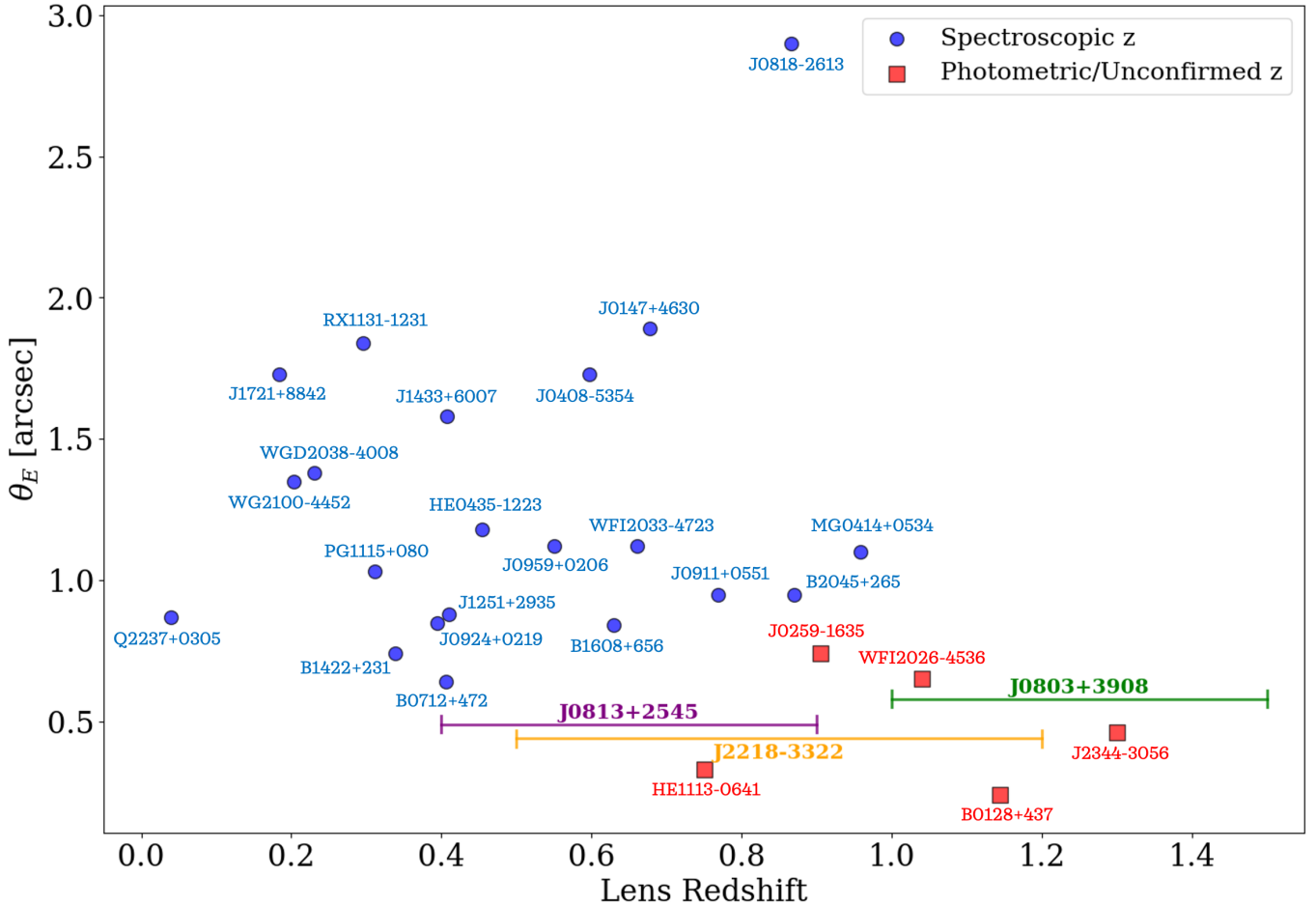


Figure 11. Lens redshifts and Einstein radii θ_E of lensing galaxies of known quadruply lensed quasars. Previously discovered objects are plotted with dots and squares. The three targets in this work are plotted with barred colored horizontal lines. See Appendix for a complete list of objects shown and corresponding reference.

seem to often have bottom-heavy initial mass functions dominated by low-mass stars (Conroy & van Dokkum 2012; Bernardi et al. 2018). In these populations, stars below $0.5 M_\odot$ could contribute up to $\sim 50\%$ of stellar mass, yet only contributing to 1% of total light output (Weidner et al. 2013). Follow-up observations, for example, spectroscopy and stellar velocity dispersion measurements on this lens, are needed to determine which scenario is the most plausible.

5.2. Quasar Host Galaxies

We are conservative about making statements regarding host galaxies for the lensed quasars, especially for the JWST targets due to the PSF mismatch. That said, there is an interesting pattern for both JWST objects in Fig. 5 and Fig. 6 that the residuals along the Einstein ring show reverse signs at different segments. For example, in Fig. 5, the residuals between lensed image B and D at the northeast of the figure have a positive sign, while the residuals between image A and C as well as A and B are largely negative. This spatial variation

of residual sign could imply that the source quasar is not located at the center of the host galaxy, because the Lenstronomy fits assume that the quasar and the host are co-centered. Several mechanisms could result in a displaced quasar. Before a binary of SMBHs coalesce, they emit anisotropic gravitational wave radiations which would result in a "recoil kick" to the merged SMBH and cause it to drift away from the host galaxy center (Favata et al. 2004; Merritt & Milosavljević 2005). Orbital dynamics of SMBH binaries (Komossa 2006), asymmetric jets (Shklovsky 1982), and tidal perturbations from external companions (Lena et al. 2014) are suggested to explain the quasar-host spatial offset as well. A galaxy in the process of merging with one black hole active would also appear lopsided (Barrows et al. 2017). An improved PSF model might be needed to investigate the detailed properties of these quasar hosts.

5.3. Degeneracy of Lensing Models

The comparison between results given by Lenstronomy and the alternative analytical model by

[Luhtaru et al. \(2021\)](#) highlights the variety/degeneracy in lensing models. It is long known that the observed configuration of a strong lensing event i.e. lensed image positions, flux ratios etc. could be reproduced by different lensing models (e.g. the mass-sheet degeneracy; [Falco et al. 1985](#); [Schneider & Sluse 2013](#)). Although both [Lenstronomy](#) and the analytical model adopt an isothermal lensing mass/potential (with external shear), their underlying assumptions are not identical. One key difference is that the analytical model does not require the lensing potential to be centered on the lensing galaxy unlike what most lens modeling codes like [Lenstronomy](#) do ([Schechter & Luhtaru 2024](#)). Rather, the model predicts that the lensing potential center lies on the Witt’s hyperbola somewhere with a small but non-zero offset (typically $\sim 0.01''$) to the lensing galaxy. This implies either: i) the potential is intrinsically displaced from the lensing galaxy (as seen in many bright cluster galaxies e.g. [Skibba et al. 2011](#)), or ii) the true potential is more intricate than the model’s prediction. We observe such offsets in the fits for all three targets in this work. The discrepancy between structural parameters by this model and the [Lenstronomy](#)-fitted results seems to favor the first scenario of a difference in the geometry of lensing potential and observed shape for each lens, emphasizing the complexity of realistic galaxies.

5.4. Comparison with Known Quad Lenses

Fig. 11 illustrates the distribution of lens redshift and Einstein radius of lensing galaxies for quadruply lensed quasars and demonstrates how our lenses fit into the population. It contains 26 of all 27 lensing galaxies in known quads with published measurements on lens redshift by far (we exclude J1004+4112 which is a cluster lens and thus has a large Einstein radius of $8.14''$) along with the three lenses in this work. The lens redshifts are scattered across $z = 0.0 \sim 1.4$ with a mean at $z = 0.592$. The Einstein radii θ_E vary between $0.25'' \sim 3.00''$ with a mean of $1.12''$, while the majority are above $0.60''$. Our three lenses are located at the lower end of the distribution of θ_E . In terms of redshift, the expected redshift ranges for both J2218-3322 and J0813+2545 lie within this distribution well. J0803+3908 is on the higher end of lens redshift in this quad lens sample set along with very few others at $z \geq 1$.

It is noteworthy that lenses with similar Einstein radii with our samples in Fig. 11 tend to have photometric or uncertain redshifts. This highlights the observational challenge for obtaining spectroscopic measurements on small-separation quads and lenses, especially with ground-based instruments. Atmospheric seeing limits the resolvability of ground telescope on subarc-

sec separation sources. That said, some current space observatories such as JWST NIRSpec already offer sufficient capacity probing these targets. Upcoming space missions such as Euclid and Roman ([Weiner et al. 2020](#); [Pearce-Casey et al. 2025](#)) would probe deeper into this largely unexplored regime, resolving lenses with smaller separations (i.e. lower enclosed mass) and/or at higher redshift. Such lenses at earlier cosmic epochs might not necessarily be similar to the contemporary population. As we approach cosmic noon, field galaxies contain more young, bright galaxies with intense star formation. While massive early-types would still be the dominating type due to their more favorable surface density configurations, we can expect to detect more late-type/edge-on and lower-mass galaxies as strong lenses. These objects would greatly advance our understanding of mass assembly history of early galaxies.

6. CONCLUSION

We present optical imaging for three quadruply lensed quasars at cosmic noon: J2218-3322 with HST/WFC3, MQJ0803+3908 with JWST/NIRCam, and SDSSJ0813+2545 with JWST/NIRCam. With numerical modelings of these systems using [Lenstronomy](#), we retrieve vital information about each of these quads, and perform aperture photometry to constrain the possible redshifts to each lensing galaxy. Our key results include:

1. [Lenstronomy](#) yields compatible image reconstructions for all three systems, with best-fit $\chi^2_\nu = 1.21, 3.87$, and 4.56 . The sub-optimal fits for the two JWST quads are mostly due to mismatch of PSF models caused by the complex diffraction patterns of NIRCam.
2. The three lenses are all compact systems with Einstein radii of $0.44'', 0.58'',$ and $0.49''$. The most probable redshift range for each one is $0.5 < z < 1.2$, $1.0 < z < 1.5$, and $0.4 < z < 0.9$, respectively.
3. The three lenses are all likely early-type galaxies given their $n_{\text{Sérsic}} \sim 4$ light profile and modest R_e around a few kpc. Compared to other lensing galaxies for quadruply lensed quasars, they have an uncommonly compact Einstein radius below $1''$. These objects vary drastically in terms of mass, color, and luminosity, together forming a diverse subset of the lensing galaxy population.

Our work exhibits a rich ecosystem of single-galaxy lenses where galaxies with distinct characteristics are all capable of producing strong gravitational lensing, and peeks into the exciting realm of subarcsec separation

strong lenses that remains under-studied so far. Upcoming surveys on next-generation instruments, including both ground-based observatories such as the Legacy Survey of Space and Time program on the Vera C. Rubin Observatory (Shajib et al. 2025) and space telescopes like the Euclid and Roman missions could expectedly expand the sample size of strong lenses by orders of magnitude, while each of them would be observed with unprecedented resolutions and depths (Oguri & Marshall 2010). Our work showcases a workflow on dealing with the rich complex details from each strong lensing system, which can yield new insights that will lead to extraordinary advancements from the current understandings on single-galaxy strong lensing, as well as the broader paradigm of galaxy formation and evolution.

ACKNOWLEDGMENTS

Observations used for this work were conducted with the NASA/ESA *Hubble Space Telescope* and *James Webb Space Telescope* and acquired from the Space Telescope Science Institute, operated by the Associa-

tion of Universities for Research in Astronomy, Inc., under NASA contract NAS 5-26555. Support for program JWST-GO-04204 was provided by NASA through a grant from the Space Telescope Science Institute, which is operated by the Association of Universities for Research in Astronomy, Inc., under NASA contract NAS 5-03127. M.L. acknowledges support from Space@Hopkins. N.L.Z. thanks the Institute for Advanced Study in Princeton, NJ for hospitality and support during regular visits, and thanks P. Schechter for many useful conversations. X.L. acknowledges support by NSF grant AST-2108162. This work utilizes `Lenstronomy` (Birrer & Amara 2018), `emcee` (Foreman-Mackey et al. 2013), `fastell` (Barkana 1999), `numpy` (Harris et al. 2020), `scipy` (Virtanen et al. 2020), `astropy` (Astropy Collaboration et al. 2018), `photutils` (Bradley et al. 2025), and `matplotlib` (Hunter 2007).

DATA

All the *HST* and *JWST* data used in this paper can be found in MAST: [10.17909/921v-5j15](https://doi.org/10.17909/921v-5j15).

REFERENCES

Agnello, A. 2018, Research Notes of the American Astronomical Society, 2, 42, doi: [10.3847/2515-5172/aac77b](https://doi.org/10.3847/2515-5172/aac77b)

Agnello, A., Grillo, C., Jones, T., et al. 2018a, MNRAS, 474, 3391, doi: [10.1093/mnras/stx2950](https://doi.org/10.1093/mnras/stx2950)

Agnello, A., & Spinelli, C. 2019, MNRAS, 489, 2525, doi: [10.1093/mnras/stz2200](https://doi.org/10.1093/mnras/stz2200)

Agnello, A., Lin, H., Buckley-Geer, L., et al. 2017, MNRAS, 472, 4038, doi: [10.1093/mnras/stx2242](https://doi.org/10.1093/mnras/stx2242)

Agnello, A., Lin, H., Kuropatkin, N., et al. 2018b, MNRAS, 479, 4345, doi: [10.1093/mnras/sty1419](https://doi.org/10.1093/mnras/sty1419)

Anguita, T., Faure, C., Kneib, J.-P., et al. 2009, A&A, 507, 35, doi: [10.1051/0004-6361/200912091](https://doi.org/10.1051/0004-6361/200912091)

Astropy Collaboration, Price-Whelan, A. M., Sipőcz, B. M., et al. 2018, AJ, 156, 123, doi: [10.3847/1538-3881/aabc4f](https://doi.org/10.3847/1538-3881/aabc4f)

Auger, M. W., Treu, T., Bolton, A. S., et al. 2009, ApJ, 705, 1099, doi: [10.1088/0004-637X/705/2/1099](https://doi.org/10.1088/0004-637X/705/2/1099)

—. 2010, ApJ, 724, 511, doi: [10.1088/0004-637X/724/1/511](https://doi.org/10.1088/0004-637X/724/1/511)

Bade, N., Siebert, J., Lopez, S., Voges, W., & Reimers, D. 1997, A&A, 317, L13

Bar-Kana, R. 1996, ApJ, 468, 17, doi: [10.1086/177666](https://doi.org/10.1086/177666)

Barkana, R. 1999, FASTELL: Fast calculation of a family of elliptical mass gravitational lens models, *Astrophysics Source Code Library*, record ascl:9910.003

Barrows, R. S., Comerford, J. M., Greene, J. E., & Pooley, D. 2017, ApJ, 838, 129, doi: [10.3847/1538-4357/aa64d9](https://doi.org/10.3847/1538-4357/aa64d9)

Begelman, M. C., Blandford, R. D., & Rees, M. J. 1980, Nature, 287, 307, doi: [10.1038/287307a0](https://doi.org/10.1038/287307a0)

Berghea, C. T., Nelson, G. J., Rusu, C. E., Keeton, C. R., & Dudik, R. P. 2017, ApJ, 844, 90, doi: [10.3847/1538-4357/aa7aa6](https://doi.org/10.3847/1538-4357/aa7aa6)

Bernardi, M., Sheth, R. K., Fischer, J. L., et al. 2018, MNRAS, 475, 757, doi: [10.1093/mnras/stx3171](https://doi.org/10.1093/mnras/stx3171)

Birrer, S., & Amara, A. 2018, Physics of the Dark Universe, 22, 189, doi: [10.1016/j.dark.2018.11.002](https://doi.org/10.1016/j.dark.2018.11.002)

Blackburne, J. A., Wisotzki, L., & Schechter, P. L. 2008, AJ, 135, 374, doi: [10.1088/0004-6256/135/1/374](https://doi.org/10.1088/0004-6256/135/1/374)

Bolton, A. S., Burles, S., Koopmans, L. V. E., et al. 2008, ApJ, 682, 964, doi: [10.1086/589327](https://doi.org/10.1086/589327)

Bolton, A. S., Burles, S., Koopmans, L. V. E., Treu, T., & Moustakas, L. A. 2006, ApJ, 638, 703, doi: [10.1086/498884](https://doi.org/10.1086/498884)

Bolton, A. S., Brownstein, J. R., Kochanek, C. S., et al. 2012, ApJ, 757, 82, doi: [10.1088/0004-637X/757/1/82](https://doi.org/10.1088/0004-637X/757/1/82)

Bradley, L., Sipőcz, B., Robitaille, T., et al. 2025, `astropy/photutils`: 2.2.0, 2.2.0, Zenodo, doi: [10.5281/zenodo.14889440](https://doi.org/10.5281/zenodo.14889440)

Broadhurst, T., & Lehar, J. 1995, ApJL, 450, L41, doi: [10.1086/316774](https://doi.org/10.1086/316774)

Buckley-Geer, E. J., Lin, H., Rusu, C. E., et al. 2020, MNRAS, 498, 3241, doi: [10.1093/mnras/staa2563](https://doi.org/10.1093/mnras/staa2563)

Cao, S., Biesiada, M., Gavazzi, R., Piórkowska, A., & Zhu, Z.-H. 2015, *ApJ*, 806, 185, doi: [10.1088/0004-637X/806/2/185](https://doi.org/10.1088/0004-637X/806/2/185)

Cappellari, M., Scott, N., Alatalo, K., et al. 2013a, *MNRAS*, 432, 1709, doi: [10.1093/mnras/stt562](https://doi.org/10.1093/mnras/stt562)

Cappellari, M., McDermid, R. M., Alatalo, K., et al. 2013b, *MNRAS*, 432, 1862, doi: [10.1093/mnras/stt644](https://doi.org/10.1093/mnras/stt644)

Cappellari, M., Romanowsky, A. J., Brodie, J. P., et al. 2015, *ApJL*, 804, L21, doi: [10.1088/2041-8205/804/1/L21](https://doi.org/10.1088/2041-8205/804/1/L21)

Chambers, K. C., Magnier, E. A., Metcalfe, N., et al. 2016, arXiv e-prints, arXiv:1612.05560, doi: [10.48550/arXiv.1612.05560](https://doi.org/10.48550/arXiv.1612.05560)

Chan, J. H. H., Schive, H.-Y., Wong, S.-K., Chiueh, T., & Broadhurst, T. 2020, *PhRvL*, 125, 111102, doi: [10.1103/PhysRevLett.125.111102](https://doi.org/10.1103/PhysRevLett.125.111102)

Chen, Y.-C., Gross, A. C., Liu, X., et al. 2025, *ApJ*, 988, 126, doi: [10.3847/1538-4357/ade23b](https://doi.org/10.3847/1538-4357/ade23b)

Chen, Y.-C., Hwang, H.-C., Shen, Y., et al. 2022, *ApJ*, 925, 162, doi: [10.3847/1538-4357/ac401b](https://doi.org/10.3847/1538-4357/ac401b)

Christian, C. A., Crabtree, D., & Waddell, P. 1987, *ApJ*, 312, 45, doi: [10.1086/164847](https://doi.org/10.1086/164847)

Combes, F., Young, L. M., & Bureau, M. 2007, *MNRAS*, 377, 1795, doi: [10.1111/j.1365-2966.2007.11759.x](https://doi.org/10.1111/j.1365-2966.2007.11759.x)

Conroy, C., & van Dokkum, P. G. 2012, *ApJ*, 760, 71, doi: [10.1088/0004-637X/760/1/71](https://doi.org/10.1088/0004-637X/760/1/71)

Dutton, A. A., & Treu, T. 2014, *MNRAS*, 438, 3594, doi: [10.1093/mnras/stt2489](https://doi.org/10.1093/mnras/stt2489)

Dux, F., Millon, M., Lemon, C., et al. 2025, *A&A*, 694, A300, doi: [10.1051/0004-6361/202452970](https://doi.org/10.1051/0004-6361/202452970)

Eigenbrod, A., Courbin, F., Meylan, G., Vuissoz, C., & Magain, P. 2006, *A&A*, 451, 759, doi: [10.1051/0004-6361:20054454](https://doi.org/10.1051/0004-6361:20054454)

Ertl, S., Schuldt, S., Suyu, S. H., et al. 2023, *A&A*, 672, A2, doi: [10.1051/0004-6361/202244909](https://doi.org/10.1051/0004-6361/202244909)

Etherington, A., Nightingale, J. W., Massey, R., et al. 2024, *MNRAS*, 531, 3684, doi: [10.1093/mnras/stae1375](https://doi.org/10.1093/mnras/stae1375)

Falco, E. E., Gorenstein, M. V., & Shapiro, I. I. 1985, *ApJL*, 289, L1, doi: [10.1086/184422](https://doi.org/10.1086/184422)

Fassnacht, C. D., Pearson, T. J., Readhead, A. C. S., et al. 1999a, *ApJ*, 527, 498, doi: [10.1086/308118](https://doi.org/10.1086/308118)

Fassnacht, C. D., Blandford, R. D., Cohen, J. G., et al. 1999b, *AJ*, 117, 658, doi: [10.1086/300724](https://doi.org/10.1086/300724)

Favata, M., Hughes, S. A., & Holz, D. E. 2004, *ApJL*, 607, L5, doi: [10.1086/421552](https://doi.org/10.1086/421552)

Fischer, P., Schade, D., & Barrientos, L. F. 1998, *ApJL*, 503, L127, doi: [10.1086/311555](https://doi.org/10.1086/311555)

Foreman-Mackey, D., Hogg, D. W., Lang, D., & Goodman, J. 2013, *PASP*, 125, 306, doi: [10.1086/670067](https://doi.org/10.1086/670067)

Gabasch, A., Bender, R., Seitz, S., et al. 2004, *A&A*, 421, 41, doi: [10.1051/0004-6361:20035909](https://doi.org/10.1051/0004-6361:20035909)

George, K. 2017, *A&A*, 598, A45, doi: [10.1051/0004-6361/201629667](https://doi.org/10.1051/0004-6361/201629667)

Gilman, D., Zhong, Y.-M., & Bovy, J. 2023, *PhRvD*, 107, 103008, doi: [10.1103/PhysRevD.107.103008](https://doi.org/10.1103/PhysRevD.107.103008)

Glikman, E., Rusu, C. E., Chen, G. C.-F., et al. 2023, *ApJ*, 943, 25, doi: [10.3847/1538-4357/aca093](https://doi.org/10.3847/1538-4357/aca093)

Gnedin, O. Y., Kravtsov, A. V., Klypin, A. A., & Nagai, D. 2004, *ApJ*, 616, 16, doi: [10.1086/424914](https://doi.org/10.1086/424914)

Graham, A. W. 2002, *MNRAS*, 334, 721, doi: [10.1046/j.1365-8711.2002.05355.x](https://doi.org/10.1046/j.1365-8711.2002.05355.x)

Gross, A. C., Chen, Y.-C., Oguri, M., et al. 2025, *The Astrophysical Journal*, 989, 112, doi: [10.3847/1538-4357/ade671](https://doi.org/10.3847/1538-4357/ade671)

Hagen, H. J., Engels, D., & Reimers, D. 1999, *A&AS*, 134, 483, doi: [10.1051/aas:1999442](https://doi.org/10.1051/aas:1999442)

Hagen, H. J., Groote, D., Engels, D., & Reimers, D. 1995, *A&AS*, 111, 195

Harris, C. R., Millman, K. J., van der Walt, S. J., et al. 2020, *Nature*, 585, 357, doi: [10.1038/s41586-020-2649-2](https://doi.org/10.1038/s41586-020-2649-2)

He, Z., Li, R., Shu, Y., et al. 2025, *ApJ*, 981, 168, doi: [10.3847/1538-4357/adaf28](https://doi.org/10.3847/1538-4357/adaf28)

Hernquist, L. 1990, *ApJ*, 356, 359, doi: [10.1086/168845](https://doi.org/10.1086/168845)

Hewitt, J. N., Turner, E. L., Lawrence, C. R., Schneider, D. P., & Brody, J. P. 1992, *AJ*, 104, 968, doi: [10.1086/116290](https://doi.org/10.1086/116290)

Hezaveh, Y. D., Dalal, N., Marrone, D. P., et al. 2016, *ApJ*, 823, 37, doi: [10.3847/0004-637X/823/1/37](https://doi.org/10.3847/0004-637X/823/1/37)

Hopkins, P. F., Hernquist, L., Cox, T. J., & Kereš, D. 2008, *ApJS*, 175, 356, doi: [10.1086/524362](https://doi.org/10.1086/524362)

Hsueh, J.-W., Oldham, L., Spingola, C., et al. 2017, *MNRAS*, 469, 3713, doi: [10.1093/mnras/stx1082](https://doi.org/10.1093/mnras/stx1082)

Hu, W., Barkana, R., & Gruzinov, A. 2000, *PhRvL*, 85, 1158, doi: [10.1103/PhysRevLett.85.1158](https://doi.org/10.1103/PhysRevLett.85.1158)

Huang, X., Storfer, C., Ravi, V., et al. 2020, *ApJ*, 894, 78, doi: [10.3847/1538-4357/ab7ff](https://doi.org/10.3847/1538-4357/ab7ff)

Hunter, J. D. 2007, *Computing in Science and Engineering*, 9, 90, doi: [10.1109/MCSE.2007.55](https://doi.org/10.1109/MCSE.2007.55)

Hwang, H.-C., Shen, Y., Zakamska, N., & Liu, X. 2020, *ApJ*, 888, 73, doi: [10.3847/1538-4357/ab5c1a](https://doi.org/10.3847/1538-4357/ab5c1a)

Impey, C. D., Falco, E. E., Kochanek, C. S., et al. 1998, *ApJ*, 509, 551, doi: [10.1086/306521](https://doi.org/10.1086/306521)

Inada, N., Becker, R. H., Burles, S., et al. 2003, *AJ*, 126, 666, doi: [10.1086/375906](https://doi.org/10.1086/375906)

Inada, N., Oguri, M., Becker, R. H., et al. 2008, *AJ*, 135, 496, doi: [10.1088/0004-6256/135/2/496](https://doi.org/10.1088/0004-6256/135/2/496)

Jackson, N., Tagore, A. S., Roberts, C., et al. 2015, *MNRAS*, 454, 287, doi: [10.1093/mnras/stv1982](https://doi.org/10.1093/mnras/stv1982)

Jackson, N., Nair, S., Browne, I. W. A., et al. 1998, *MNRAS*, 296, 483, doi: [10.1046/j.1365-8711.1998.01304.x](https://doi.org/10.1046/j.1365-8711.1998.01304.x)

Kamionkowski, M., & Riess, A. G. 2023, Annual Review of Nuclear and Particle Science, 73, 153, doi: [10.1146/annurev-nucl-111422-024107](https://doi.org/10.1146/annurev-nucl-111422-024107)

Kaplinghat, M., Keeley, R. E., Linden, T., & Yu, H.-B. 2014, PhRvL, 113, 021302, doi: [10.1103/PhysRevLett.113.021302](https://doi.org/10.1103/PhysRevLett.113.021302)

Kayo, I., Inada, N., Oguri, M., et al. 2007, AJ, 134, 1515, doi: [10.1086/521652](https://doi.org/10.1086/521652)

Keeton, C. R. 2001, arXiv e-prints, astro, doi: [10.48550/arXiv.astro-ph/0102341](https://doi.org/10.48550/arXiv.astro-ph/0102341)

Keeton, C. R., Burles, S., Schechter, P. L., & Wambsganss, J. 2006, ApJ, 639, 1, doi: [10.1086/499264](https://doi.org/10.1086/499264)

Keeton, C. R., & Kochanek, C. S. 1998, ApJ, 495, 157, doi: [10.1086/305272](https://doi.org/10.1086/305272)

Keeton, C. R., Kochanek, C. S., & Falco, E. E. 1998, ApJ, 509, 561, doi: [10.1086/306502](https://doi.org/10.1086/306502)

Knox, L., & Millea, M. 2020, PhRvD, 101, 043533, doi: [10.1103/PhysRevD.101.043533](https://doi.org/10.1103/PhysRevD.101.043533)

Kochanek, C. S., & Apostolakis, J. 1988, MNRAS, 235, 1073, doi: [10.1093/mnras/235.4.1073](https://doi.org/10.1093/mnras/235.4.1073)

Komossa, S. 2006, Mem. Soc. Astron. Italiana, 77, 733

Koopmans, L. V. E., Treu, T., Bolton, A. S., Burles, S., & Moustakas, L. A. 2006, ApJ, 649, 599, doi: [10.1086/505696](https://doi.org/10.1086/505696)

Koopmans, L. V. E., Bolton, A., Treu, T., et al. 2009, ApJL, 703, L51, doi: [10.1088/0004-637X/703/1/L51](https://doi.org/10.1088/0004-637X/703/1/L51)

Kormann, R., Schneider, P., & Bartelmann, M. 1994a, A&A, 284, 285

—. 1994b, A&A, 286, 357, doi: [10.48550/arXiv.astro-ph/9311011](https://doi.org/10.48550/arXiv.astro-ph/9311011)

Lagattuta, D. J., Auger, M. W., & Fassnacht, C. D. 2010, ApJL, 716, L185, doi: [10.1088/2041-8205/716/2/L185](https://doi.org/10.1088/2041-8205/716/2/L185)

Lagattuta, D. J., Vegetti, S., Fassnacht, C. D., et al. 2012, MNRAS, 424, 2800, doi: [10.1111/j.1365-2966.2012.21406.x](https://doi.org/10.1111/j.1365-2966.2012.21406.x)

Larache, A., Gilman, D., Li, X., Bovy, J., & Du, X. 2022, MNRAS, 517, 1867, doi: [10.1093/mnras/stac2677](https://doi.org/10.1093/mnras/stac2677)

Lemon, C. A., Auger, M. W., McMahon, R. G., & Koposov, S. E. 2017, MNRAS, 472, 5023, doi: [10.1093/mnras/stx2094](https://doi.org/10.1093/mnras/stx2094)

Lemon, C. A., Auger, M. W., McMahon, R. G., & Ostrovski, F. 2018, MNRAS, 479, 5060, doi: [10.1093/mnras/sty911](https://doi.org/10.1093/mnras/sty911)

Lena, D., Robinson, A., Marconi, A., et al. 2014, ApJ, 795, 146, doi: [10.1088/0004-637X/795/2/146](https://doi.org/10.1088/0004-637X/795/2/146)

Li, P., McGaugh, S. S., Lelli, F., Schombert, J. M., & Pawlowski, M. S. 2022, A&A, 665, A143, doi: [10.1051/0004-6361/202243916](https://doi.org/10.1051/0004-6361/202243916)

Lin, H., Buckley-Geer, E., Agnello, A., et al. 2017, ApJL, 838, L15, doi: [10.3847/2041-8213/aa624e](https://doi.org/10.3847/2041-8213/aa624e)

Liu, X., Greene, J. E., Shen, Y., & Strauss, M. A. 2010, ApJL, 715, L30, doi: [10.1088/2041-8205/715/1/L30](https://doi.org/10.1088/2041-8205/715/1/L30)

Lucey, J. R., Schechter, P. L., Smith, R. J., & Anguita, T. 2018, MNRAS, 476, 927, doi: [10.1093/mnras/sty243](https://doi.org/10.1093/mnras/sty243)

Luhtaru, R., Schechter, P. L., & de Soto, K. M. 2021, ApJ, 915, 4, doi: [10.3847/1538-4357/abfda1](https://doi.org/10.3847/1538-4357/abfda1)

Magain, P., Surdej, J., Swings, J.-P., Borgeest, U., & Kayser, R. 1988, Nature, 334, 325, doi: [10.1038/334325a0](https://doi.org/10.1038/334325a0)

Mao, S., & Schneider, P. 1998, MNRAS, 295, 587, doi: [10.1046/j.1365-8711.1998.01319.x](https://doi.org/10.1046/j.1365-8711.1998.01319.x)

Mateos, S., Alonso-Herrero, A., Carrera, F. J., et al. 2012, MNRAS, 426, 3271, doi: [10.1111/j.1365-2966.2012.21843.x](https://doi.org/10.1111/j.1365-2966.2012.21843.x)

McKean, J. P., Koopmans, L. V. E., Flack, C. E., et al. 2007, MNRAS, 378, 109, doi: [10.1111/j.1365-2966.2007.11744.x](https://doi.org/10.1111/j.1365-2966.2007.11744.x)

Merritt, D., & Milosavljević, M. 2005, Living Reviews in Relativity, 8, 8, doi: [10.12942/lrr-2005-8](https://doi.org/10.12942/lrr-2005-8)

Metcalf, R. B., Meneghetti, M., Avestruz, C., et al. 2019, A&A, 625, A119, doi: [10.1051/0004-6361/201832797](https://doi.org/10.1051/0004-6361/201832797)

Meylan, G., Jetzer, P., & North, P., eds. 2006, Gravitational Lensing: Strong, Weak and Micro, ed. G. Meylan, P. Jetzer, & P. North

Minezaki, T., Chiba, M., Kashikawa, N., Inoue, K. T., & Kataza, H. 2009, ApJ, 697, 610, doi: [10.1088/0004-637X/697/1/610](https://doi.org/10.1088/0004-637X/697/1/610)

Morgan, N. D., Caldwell, J. A. R., Schechter, P. L., et al. 2004, AJ, 127, 2617, doi: [10.1086/383295](https://doi.org/10.1086/383295)

Mozumdar, P., Fassnacht, C. D., Treu, T., Spinello, C., & Shajib, A. J. 2023, A&A, 672, A20, doi: [10.1051/0004-6361/202245082](https://doi.org/10.1051/0004-6361/202245082)

Myers, S. T., Rusin, D., Fassnacht, C. D., et al. 1999, AJ, 117, 2565, doi: [10.1086/300875](https://doi.org/10.1086/300875)

Navarro, J. F., Frenk, C. S., & White, S. D. M. 1997, ApJ, 490, 493, doi: [10.1086/304888](https://doi.org/10.1086/304888)

Nishikawa, H., Boddy, K. K., & Kaplinghat, M. 2020, PhRvD, 101, 063009, doi: [10.1103/PhysRevD.101.063009](https://doi.org/10.1103/PhysRevD.101.063009)

Oguri, M. 2010, PASJ, 62, 1017, doi: [10.1093/pasj/62.4.1017](https://doi.org/10.1093/pasj/62.4.1017)

—. 2021, PASP, 133, 074504, doi: [10.1088/1538-3873/ac12db](https://doi.org/10.1088/1538-3873/ac12db)

Oguri, M., Inada, N., Blackburne, J. A., et al. 2008, MNRAS, 391, 1973, doi: [10.1111/j.1365-2966.2008.14032.x](https://doi.org/10.1111/j.1365-2966.2008.14032.x)

Oguri, M., & Marshall, P. J. 2010, MNRAS, 405, 2579, doi: [10.1111/j.1365-2966.2010.16639.x](https://doi.org/10.1111/j.1365-2966.2010.16639.x)

Patnaik, A. R., Browne, I. W. A., Walsh, D., Chaffee, F. H., & Foltz, C. B. 1992, MNRAS, 259, 1P, doi: [10.1093/mnras/259.1.1P](https://doi.org/10.1093/mnras/259.1.1P)

Pearce-Casey, R., Nagam, B. C., Wilde, J., et al. 2025, *A&A*, 696, A214, doi: [10.1051/0004-6361/202453152](https://doi.org/10.1051/0004-6361/202453152)

Perrin, M. D., Soummer, R., Elliott, E. M., Lallo, M. D., & Sivaramakrishnan, A. 2012, in Society of Photo-Optical Instrumentation Engineers (SPIE) Conference Series, Vol. 8442, Space Telescopes and Instrumentation 2012: Optical, Infrared, and Millimeter Wave, ed. M. C. Clampin, G. G. Fazio, H. A. MacEwen, & J. M. Oschmann, Jr., 84423D, doi: [10.1117/12.925230](https://doi.org/10.1117/12.925230)

Phillips, P. M., Norbury, M. A., Koopmans, L. V. E., et al. 2000, *MNRAS*, 319, L7, doi: [10.1046/j.1365-8711.2000.04033.x](https://doi.org/10.1046/j.1365-8711.2000.04033.x)

Planck Collaboration, Aghanim, N., Akrami, Y., et al. 2020, *A&A*, 641, A6, doi: [10.1051/0004-6361/201833910](https://doi.org/10.1051/0004-6361/201833910)

Ratnatunga, K. U., Griffiths, R. E., & Ostrander, E. J. 1999, *AJ*, 117, 2010, doi: [10.1086/300840](https://doi.org/10.1086/300840)

Reimers, D., Hagen, H. J., Baade, R., Lopez, S., & Tytler, D. 2002, *A&A*, 382, L26, doi: [10.1051/0004-6361:20011798](https://doi.org/10.1051/0004-6361:20011798)

Reimers, D., & Wisotzki, L. 1997, *The Messenger*, 88, 14

Riess, A. G., Casertano, S., Yuan, W., et al. 2021, *ApJL*, 908, L6, doi: [10.3847/2041-8213/abdbaf](https://doi.org/10.3847/2041-8213/abdbaf)

Riess, A. G., Macri, L. M., Hoffmann, S. L., et al. 2016, *ApJ*, 826, 56, doi: [10.3847/0004-637X/826/1/56](https://doi.org/10.3847/0004-637X/826/1/56)

Riess, A. G., Yuan, W., Macri, L. M., et al. 2022, *ApJL*, 934, L7, doi: [10.3847/2041-8213/ac5c5b](https://doi.org/10.3847/2041-8213/ac5c5b)

Robertson, A., Massey, R., Eke, V., Schaye, J., & Theuns, T. 2021, *MNRAS*, 501, 4610, doi: [10.1093/mnras/staa3954](https://doi.org/10.1093/mnras/staa3954)

Rodriguez, C., Taylor, G. B., Zavala, R. T., et al. 2006, *ApJ*, 646, 49, doi: [10.1086/504825](https://doi.org/10.1086/504825)

Rowan-Robinson, M., Broadhurst, T., Lawrence, A., et al. 1991, *Nature*, 351, 719, doi: [10.1038/351719a0](https://doi.org/10.1038/351719a0)

Rusin, D., Kochanek, C. S., Norbury, M., et al. 2001, *ApJ*, 557, 594, doi: [10.1086/322251](https://doi.org/10.1086/322251)

Rusu, C. E., Oguri, M., Minowa, Y., et al. 2016, *MNRAS*, 458, 2, doi: [10.1093/mnras/stw092](https://doi.org/10.1093/mnras/stw092)

Saha, P., Sluse, D., Wagner, J., & Williams, L. L. R. 2024, *SSRv*, 220, 12, doi: [10.1007/s11214-024-01041-w](https://doi.org/10.1007/s11214-024-01041-w)

Salpeter, E. E. 1955, *ApJ*, 121, 161, doi: [10.1086/145971](https://doi.org/10.1086/145971)

Schechter, P. L. 2003, arXiv e-prints, astro, doi: [10.48550/arXiv.astro-ph/0304480](https://doi.org/10.48550/arXiv.astro-ph/0304480)

Schechter, P. L., Anguita, T., Morgan, N. D., Read, M., & Shanks, T. 2018, *Research Notes of the American Astronomical Society*, 2, 21, doi: [10.3847/2515-5172/aac1bf](https://doi.org/10.3847/2515-5172/aac1bf)

Schechter, P. L., & Luhtaru, R. 2024, *ApJ*, 975, 62, doi: [10.3847/1538-4357/ad7f4d](https://doi.org/10.3847/1538-4357/ad7f4d)

Schechter, P. L., Morgan, N. D., Chehade, B., et al. 2017, *AJ*, 153, 219, doi: [10.3847/1538-3881/aa6899](https://doi.org/10.3847/1538-3881/aa6899)

Schechter, P. L., & Wambsganss, J. 2002, *ApJ*, 580, 685, doi: [10.1086/343856](https://doi.org/10.1086/343856)

Schindler, J.-T., Fan, X., McGreer, I. D., et al. 2018, *ApJ*, 863, 144, doi: [10.3847/1538-4357/aad2dd](https://doi.org/10.3847/1538-4357/aad2dd)

Schive, H.-Y., Chiueh, T., & Broadhurst, T. 2014, *Nature Physics*, 10, 496, doi: [10.1038/nphys2996](https://doi.org/10.1038/nphys2996)

Schmidt, T., Treu, T., Birrer, S., et al. 2023, *MNRAS*, 518, 1260, doi: [10.1093/mnras/stac2235](https://doi.org/10.1093/mnras/stac2235)

Schneider, P., & Sluse, D. 2013, *A&A*, 559, A37, doi: [10.1051/0004-6361/201321882](https://doi.org/10.1051/0004-6361/201321882)

Secrest, N. J., Dudik, R. P., Dorland, B. N., et al. 2015, *ApJS*, 221, 12, doi: [10.1088/0067-0049/221/1/12](https://doi.org/10.1088/0067-0049/221/1/12)

Sersic, J. L. 1968, *Atlas de Galaxias Australes*

Shajib, A. J., Treu, T., & Agnello, A. 2018, *MNRAS*, 473, 210, doi: [10.1093/mnras/stx2302](https://doi.org/10.1093/mnras/stx2302)

Shajib, A. J., Vernardos, G., Collett, T. E., et al. 2024, *SSRv*, 220, 87, doi: [10.1007/s11214-024-01105-x](https://doi.org/10.1007/s11214-024-01105-x)

Shajib, A. J., Smith, G. P., Birrer, S., et al. 2025, *Philosophical Transactions of the Royal Society of London Series A*, 383, 20240117, doi: [10.1098/rsta.2024.0117](https://doi.org/10.1098/rsta.2024.0117)

Shen, Y., Hwang, H.-C., Zakamska, N., & Liu, X. 2019, *ApJL*, 885, L4, doi: [10.3847/2041-8213/ab4b54](https://doi.org/10.3847/2041-8213/ab4b54)

Shen, Y., Liu, X., Greene, J. E., & Strauss, M. A. 2011, *ApJ*, 735, 48, doi: [10.1088/0004-637X/735/1/48](https://doi.org/10.1088/0004-637X/735/1/48)

Shen, Y., Chen, Y.-C., Hwang, H.-C., et al. 2021, *Nature Astronomy*, 5, 569, doi: [10.1038/s41550-021-01323-1](https://doi.org/10.1038/s41550-021-01323-1)

Shen, Y., Hwang, H.-C., Oguri, M., et al. 2023, *ApJ*, 943, 38, doi: [10.3847/1538-4357/aca662](https://doi.org/10.3847/1538-4357/aca662)

Shklovsky, I. S. 1982, in *IAU Symposium*, Vol. 97, *Extragalactic Radio Sources*, ed. D. S. Heeschen & C. M. Wade, 475–481

Silva, L., Granato, G. L., Bressan, A., & Danese, L. 1998, *ApJ*, 509, 103, doi: [10.1086/306476](https://doi.org/10.1086/306476)

Skibba, R. A., van den Bosch, F. C., Yang, X., et al. 2011, *MNRAS*, 410, 417, doi: [10.1111/j.1365-2966.2010.17452.x](https://doi.org/10.1111/j.1365-2966.2010.17452.x)

Sluse, D., Chantry, V., Magain, P., Courbin, F., & Meylan, G. 2012, *A&A*, 538, A99, doi: [10.1051/0004-6361/201015844](https://doi.org/10.1051/0004-6361/201015844)

Sluse, D., Surdej, J., Claeskens, J.-F., et al. 2003, *A&A*, 406, L43, doi: [10.1051/0004-6361:20030904](https://doi.org/10.1051/0004-6361:20030904)

Sonnenfeld, A. 2024, *A&A*, 690, A325, doi: [10.1051/0004-6361/202451341](https://doi.org/10.1051/0004-6361/202451341)

Sonnenfeld, A., Li, S.-S., Despali, G., et al. 2023, *A&A*, 678, A4, doi: [10.1051/0004-6361/202346026](https://doi.org/10.1051/0004-6361/202346026)

Suyu, S. H., Marshall, P. J., Auger, M. W., et al. 2010, *ApJ*, 711, 201, doi: [10.1088/0004-637X/711/1/201](https://doi.org/10.1088/0004-637X/711/1/201)

Suyu, S. H., Marshall, P. J., Blandford, R. D., et al. 2009, *ApJ*, 691, 277, doi: [10.1088/0004-637X/691/1/277](https://doi.org/10.1088/0004-637X/691/1/277)

Suyu, S. H., Auger, M. W., Hilbert, S., et al. 2013, *ApJ*, 766, 70, doi: [10.1088/0004-637X/766/2/70](https://doi.org/10.1088/0004-637X/766/2/70)

Sygnet, J. F., Tu, H., Fort, B., & Gavazzi, R. 2010, *A&A*, 517, A25, doi: [10.1051/0004-6361/200913977](https://doi.org/10.1051/0004-6361/200913977)

Sykes, C. M., Browne, I. W. A., Jackson, N. J., et al. 1998, *MNRAS*, 301, 310, doi: [10.1046/j.1365-8711.1998.02081.x](https://doi.org/10.1046/j.1365-8711.1998.02081.x)

Tessore, N., & Metcalf, R. B. 2015, *A&A*, 580, A79, doi: [10.1051/0004-6361/201526773](https://doi.org/10.1051/0004-6361/201526773)

Treu, T. 2010, *ARA&A*, 48, 87, doi: [10.1146/annurev-astro-081309-130924](https://doi.org/10.1146/annurev-astro-081309-130924)

Treu, T., & Koopmans, L. V. E. 2004, *ApJ*, 611, 739, doi: [10.1086/422245](https://doi.org/10.1086/422245)

Treu, T., & Marshall, P. J. 2016, *A&A Rv*, 24, 11, doi: [10.1007/s00159-016-0096-8](https://doi.org/10.1007/s00159-016-0096-8)

van der Marel, R. P., & van Dokkum, P. G. 2007, *ApJ*, 668, 756, doi: [10.1086/521211](https://doi.org/10.1086/521211)

van der Wel, A., Franx, M., van Dokkum, P. G., et al. 2014, *ApJ*, 788, 28, doi: [10.1088/0004-637X/788/1/28](https://doi.org/10.1088/0004-637X/788/1/28)

Vegetti, S., Birrer, S., Despali, G., et al. 2024, *SSRv*, 220, 58, doi: [10.1007/s11214-024-01087-w](https://doi.org/10.1007/s11214-024-01087-w)

Virtanen, P., Gommers, R., Oliphant, T. E., et al. 2020, *Nature Methods*, 17, 261, doi: [10.1038/s41592-019-0686-2](https://doi.org/10.1038/s41592-019-0686-2)

Walsh, D., Carswell, R. F., & Weymann, R. J. 1979, *Nature*, 279, 381, doi: [10.1038/279381a0](https://doi.org/10.1038/279381a0)

Wambsganss, J., & Paczynski, B. 1994, *AJ*, 108, 1156, doi: [10.1086/117144](https://doi.org/10.1086/117144)

Weidner, C., Ferreras, I., Vazdekis, A., & La Barbera, F. 2013, *MNRAS*, 435, 2274, doi: [10.1093/mnras/stt1445](https://doi.org/10.1093/mnras/stt1445)

Weiner, C., Serjeant, S., & Sedgwick, C. 2020, *Research Notes of the American Astronomical Society*, 4, 190, doi: [10.3847/2515-5172/abc4ea](https://doi.org/10.3847/2515-5172/abc4ea)

Wiklind, T., Combes, F., & Kanekar, N. 2018, *ApJ*, 864, 73, doi: [10.3847/1538-4357/aad4ac](https://doi.org/10.3847/1538-4357/aad4ac)

Winn, J. N., Lovell, J. E. J., Chen, H.-W., et al. 2002, *ApJ*, 564, 143, doi: [10.1086/324144](https://doi.org/10.1086/324144)

Wisotzki, L., Christlieb, N., Liu, M. C., et al. 1999, *A&A*, 348, L41, doi: [10.48550/arXiv.astro-ph/9907227](https://doi.org/10.48550/arXiv.astro-ph/9907227)

Wisotzki, L., Schechter, P. L., Bradt, H. V., Heinmüller, J., & Reimers, D. 2002, *A&A*, 395, 17, doi: [10.1051/0004-6361:20021213](https://doi.org/10.1051/0004-6361:20021213)

Witt, H. J. 1996, *ApJL*, 472, L1, doi: [10.1086/310358](https://doi.org/10.1086/310358)

Wong, K. C., Suyu, S. H., Auger, M. W., et al. 2017, *MNRAS*, 465, 4895, doi: [10.1093/mnras/stw3077](https://doi.org/10.1093/mnras/stw3077)

Wynne, R. A., & Schechter, P. L. 2018, *arXiv e-prints*, arXiv:1808.06151, doi: [10.48550/arXiv.1808.06151](https://doi.org/10.48550/arXiv.1808.06151)

Yee, H. K. C. 1988, *AJ*, 95, 1331, doi: [10.1086/114729](https://doi.org/10.1086/114729)

APPENDIX

List of quadruply lensed quasars with known lens redshift by October 2025 (excluding the three objects from this work):

Name	z_{lens}	z_{source}	θ_E ($''$)	M_{Ein}^\dagger ($10^{11} M_\odot$)	Lens Type	Reference
B0128+437	1.145*	3.124	0.24	0.3	Spiral/S0	Phillips et al. (2000); Lagattuta et al. (2010)
J0134-0931	0.765	2.220	—	—	Pair (S + S)	Winn et al. (2002); Wiklind et al. (2018)
J0147+4630	0.678	2.377	1.89	11.2	Early-type	Berghea et al. (2017); Schmidt et al. (2023)
J0214-2105	0.450*	3.240	—	—	—	Agnello (2018)
J0230-2130	0.523	2.162	—	—	Pair (E + S?)	Wisotzki et al. (1999); Eigenbrod et al. (2006)
J0259-1635	0.905*	2.160	0.74	2.5	—	Schechter et al. (2018); Schmidt et al. (2023)
J0408-5354	0.597	2.375	1.73	6.0	Early-type	Agnello et al. (2017); Lin et al. (2017)
MG0414+0534	0.958	2.639	1.10	5.2	Elliptical	Hewitt et al. (1992); Minezaki et al. (2009)
HE0435-1223	0.454	1.693	1.18	3.2	Elliptical	Wisotzki et al. (2002); Wong et al. (2017)
B0712+472	0.406	1.339	0.64	0.9	Late-type	Jackson et al. (1998); Hsueh et al. (2017)
J0818-2613	0.866	2.155	2.90	36.4	Early-type?	Mozumdar et al. (2023); Schmidt et al. (2023)
J0911+0551	0.769	2.763	0.95	3.0	Early-type?	Bade et al. (1997); Jackson et al. (2015)
J0924+0219	0.394	1.524	0.85	1.5	Elliptical	Inada et al. (2003)
J0959+0206	0.551	3.140	0.74	1.3	—	Anguita et al. (2009); Cao et al. (2015)
J1004+4112	0.680	1.734	8.14	243.4	Elliptical + cluster	Inada et al. (2003); Oguri (2010)
FSC10214+4724	0.900*	2.286	—	—	Elliptical	Rowan-Robinson et al. (1991); Broadhurst & Lehar (1995)
J1042+1641	0.599*	2.500	—	—	Early-type	Glikman et al. (2023)
HE1113-0641	0.750*	1.235	0.33	0.7	—	Blackburne et al. (2008)
PG1115+080	0.311	1.722	1.03	1.6	Pair (E + E?)	Christian et al. (1987); Impey et al. (1998)
RXJ1131-1231	0.295	0.658	1.64	5.9	Elliptical	Sluse et al. (2003); Suyu et al. (2013)
J1138+0314	0.445	2.438	—	—	Early-type	Inada et al. (2008)
J1251+2935	0.410	0.802	0.88	2.5	Early-type	Kayo et al. (2007)
2M1310-1714	0.293	1.975	—	—	Early-type	Lucey et al. (2018)
J1330+1810	0.373	1.393	—	—	Late-type	Oguri et al. (2008); Rusu et al. (2016)
B1359+154	0.900*	3.235	1.10	4.5	Group (3 galaxies)	Myers et al. (1999); Rusin et al. (2001)
HST14113+5211	0.465	2.811	—	—	Spiral	Fischer et al. (1998); Ratnatunga et al. (1999)
H1413+117	0.940*	2.560	—	—	—	Magain et al. (1988)
B1422+231	0.339	3.620	0.74	0.8	Early-type + group	Patnaik et al. (1992); Kormann et al. (1994b)
J1433+6007	0.407	2.740	1.58	4.6	Early-type	Agnello et al. (2018a); Schmidt et al. (2023)
B1608+656	0.630	1.394	0.84	2.7	Pair (E + S)	Fassnacht et al. (1999a); Suyu et al. (2009)
J1721+8842	0.184	2.370	1.74	2.7	Pair (E + E)	Lemon et al. (2018); Dux et al. (2025)
B1933+503	0.755	2.638	—	—	Early-type	Sykes et al. (1998)
B1938+666	0.881	2.059	—	—	Early-type	Patnaik et al. (1992); Lagattuta et al. (2012)
WFI2026-4536	1.040*	2.230	0.65	2.3	—	Morgan et al. (2004); Sluse et al. (2012)
WFI2033-4723	0.661	1.662	1.12	4.6	Elliptical + group	Morgan et al. (2004); Sluse et al. (2012)
WGD2038-4008	0.230	0.777	1.38	2.7	Early-type	Agnello et al. (2018b); Buckley-Geer et al. (2020)
B2045+265	0.870	1.280	0.95	7.2	Elliptical + satellite	Fassnacht et al. (1999b); McKean et al. (2007)
WG2100-4452	0.203	0.920	1.35	2.1	—	Agnello & Spiniello (2019); Ertl et al. (2023)
Q2237+0305	0.039	1.695	0.87	0.1	Spiral	Yee (1988); Wambsganss & Paczynski (1994)
J2344-3056	1.300*	1.298	0.50	—	Elliptical?	Schechter et al. (2017); He et al. (2025)

[†] We calculate the enclosed Einstein mass manually with the redshifts and Einstein radius.

^{*} Unconfirmed or photometric redshift.

Notes: S = Spiral; E = Elliptical; S0 = Lenticular; “Early-type” includes E & S0 galaxies.

“—” indicates no information available in the literature. “?” indicates the classification is not definitive.